SHOCK-TUBE TIME-HISTORY MEASUREMENTS OF H_2O IN THE H_2/O_2 SYSTEM USING IR LASER ABSORPTION SPECTROSCOPY

A Thesis

by

CLAYTON REED MULVIHILL

Submitted to the Office of Graduate and Professional Studies of
Texas A&M University
in partial fulfillment of the requirements for the degree of

MASTER OF SCIENCE

Chair of Committee,	Eric L. Petersen
Committee Members,	Rodney D. W. Bowersox
	David A. Staack
Head of Department,	Andreas Polycarpou

May 2015

Major Subject: Mechanical Engineering

ABSTRACT

H_2O time-histories were studied within the H_2/O_2 system using a tunable diode laser system and a pressure-driven shock tube. Stoichiometric H_2/O_2 mixtures were prepared in high amounts of argon dilution. The mixtures were heated using a shock tube with a driver length of 3.04 m, a driven length of 6.78 m, and an inner diameter of 16.2 cm. A tunable diode laser (TDL) was used to measure H_2O concentration near the endwall region of the shock tube after the passage of the reflected shock wave, 1.6 cm from the endwall. Both the incident and transmitted beam intensities were measured using IR photodetectors. The laser was tuned to access the H_2O transition at 7204 cm^{-1}. Experiments in the H_2/O_2 system were performed from 1100 to 1500 K and at an average pressure of 2.8 atm. The experimental results were compared with a mechanism from Hong et al. (2011). Preliminary results show good agreement in ignition delay time between experiment and model. A computer routine was created to modify the absorption coefficient as a function of temperature to account for the temperature variation during the experiment due to the chemical reaction. After rescaling, the corrected H_2O profiles showed excellent agreement with the chemical kinetics model. Topics related to mechanism validation, the potential effects of impurities, and measurement accuracy are also addressed in the thesis.

DEDICATION

I would like to dedicate this thesis to my fiancé, Meredith. Thanks for supporting me through this time. I love you and look forward to growing more like Christ alongside you.

ACKNOWLEDGMENTS

I would like to thank my advisor, Dr. Eric Petersen, for his continued support of and dedication to my education. I would also like to thank my committee members, Drs. Rodney Bowersox and David Staack, for the time they have given to support this thesis. I would finally like to thank my colleagues in the Petersen Research Group, past and present, who have offered both advice and friendship throughout the entirety of my time with them.

NOMENCLATURE

TDL	Tunable diode laser
E	Energy [J]
h	Planck's constant [J s]
v	Frequency [Hz]
λ	Wavelength [m]
c	Speed of light [m s^{-1}]
$\bar{v}$	Wavenumber [cm^{-1}]
Q	Total partition function
k	Boltzmann's constant [J K^{-1} $molecule^{-1}$]
T	Temperature [K]
I	Transmitted light intensity [W m^{-2}]
I_0	Incident light intensity [W m^{-2}]
P	Pressure [atm]
X_{abs}	Mole fraction of absorbing species
L	Path length [cm]
k_v	Spectral absorption coefficient [cm^{-1} atm^{-1}]
$S(T)$	Line strength [cm^{-2} atm^{-1}]
$\phi(\bar{v} - \bar{v}_0)$	Line shape function [cm]
$\bar{v}_0$	Wavenumber at line center [cm^{-1}]
HWHM	Half-width at half-maximum

γ_D	Doppler (thermal) broadening HWHM [cm^{-1}]
γ_L	Lorentzian (collisional) broadening HWHM [cm^{-1}]
M	Molecular mass [kg $kmol^{-1}$]
n	Temperature broadening exponent
γ_{air}	Air-broadened HWHM at reference conditions [cm^{-1}]
γ_{self}	Self-broadened HWHM at reference conditions [cm^{-1}]
σ_v	Absorption cross-section [cm^2 $molecule^{-1}$]
γ_V	Voigt HWHM [cm^{-1}]
δ	Collisional shift parameter [cm^{-1} atm^{-1}]
N_L^0	Loschmidt constant at reference conditions [molecules cm^{-3} atm^{-1}]

TABLE OF CONTENTS

Page

LIST OF FIGURES

Page

CHAPTER I

INTRODUCTION

Chemical kinetics is the study of both the rates at which chemical reactions take place and the factors that affect these rates. These factors include the temperature and pressure of the reactants, among others. A detailed understanding of chemical kinetics has a wide range of applications, such as the prevention of auto-ignition and flashback in gas turbines. The primary tool for compiling chemical kinetics data is the chemical kinetics mechanism. This tool is a collection of first-order differential equations that describe the rate of change of species concentrations over time. Massive collections can be formed to describe complex systems of reactants with many sub-reactions. The differential equations that describe the sub-reactions can be solved simultaneously by a numerical solver. In doing so, the time-histories of the reacting species can be predicted.

Accurate rate coefficients are necessary for proper calculations of species time-histories. One well-tested method of determining rate coefficients is through the use of laser absorption spectroscopy. In this technique, the fractional attenuation of monochromatic laser light can be used to calculate the concentration of a species of interest. This concentration can be tracked during the progress of a reaction to obtain a species time-history, which can then be compared to the predictions from a chemical kinetics mechanism. If discrepancies exist between the model and the data, key rate coefficients can be adjusted accordingly to resolve these differences. The shock tube is a device that allows for high-temperature and -pressure conditions to be created behind a

reflected shock wave. These conditions can be sustained for lengths of time that are long relative to characteristic combustion timescales. This device pairs well with laser absorption spectroscopy; laser measurements can be performed within an environment that is at a known temperature and pressure.

The H_2/O_2 system is a crucial component of every hydrocarbon kinetics mechanism. Every hydrocarbon system eventually undergoes some form of H_2/O_2 reaction, and this system also contains many elementary reactions [1]. Therefore, a detailed understanding of H_2/O_2 reactions is paramount. Accordingly, several workers have studied this system in depth [2-5]. Well-known chemical kinetics mechanisms such as GRI Mech 3.0 and AramcoMech 1.1 contain within them detailed H_2/O_2 sub-mechanisms [6, 7]. Despite this effort, there discrepancies still remain in the results from each of these predictions. Even the recent results from Hong et al., though seemingly laying to rest several disagreements, mention that mechanism results had to be time-shifted to match the experimental data [2]. Clearly, a need remains for investigation into the H_2/O_2 system.

This thesis attempts to investigate some of the issues mentioned. Tests are performed upon Ar-diluted H_2/O_2 mixtures in a shock tube. Near-IR laser absorption spectroscopy near 1.4 microns is used to obtain H_2O time-histories behind reflected shock waves. The resulting time-histories are compared with the mechanism predictions from Hong et al. Also, ignition delay times are measured and compared with the same mechanism. Chapter II of this thesis addresses the background of this problem, including experimental techniques and relevant theory. Chapter III describes the methods used to

model the spectral features of H_2O and also presents the experimental setup. Chapter IV presents the results of the experiments, including time-histories and ignition delay times, and compares them to a chemical kinetics model. Chapter V suggests future problems that should be addressed and makes several recommendations as to how they could be approached. Additional experimental results are included in the Appendix.

CHAPTER II

BACKGROUND

Shock Tubes

Shock tubes allow for specific temperatures and pressures to be achieved within gaseous mixtures. Attainable temperatures range from 500 to 5,000 K, while attainable pressures range from sub-atmospheric to 500 atm [8]. This wide range of conditions facilitates a large number of applications.

The first experiments with a shock tube were performed in 1899 by the French scientist Paul Vielle, who mostly experimented with different diaphragm materials and driver gases [9]. Interestingly, Vielle actually observed deflagration-to-detonation transitions prior to discovering how to generate shock waves with no simultaneous flame front. Following Vielle's work, shock processes continued to garner interest over the next several decades, with workers developing new optical measurement techniques as well as theories on the origins of shock waves [9]. One large contributor to the area of shock waves was the British scientist Walter Payman. Payman largely focused his efforts on detonation processes in a tube [10-12] but in 1946 published a paper describing a shock tube in which non-reacting gases were used in the driven side [13]. Shock tubes continued to see further development in Europe over the following years. B.D. Henshall defended his doctoral dissertation on shock tubes at Bristol University (Great Britain) in 1952 [9]. The German scientist Hubert Schardin, one of the early pioneers of both shock

tubes and their associated measurement devices, continued to perform work as late as 1958 [9]. Several years later, British scientists A.G. Gaydon and I.R. Hurle published their compendium on shock tubes titled “The shock tube in high-temperature chemical physics” [14].

The shock tube did not remain confined to Europe but began to see use in the United States, among other nations. One of the foremost pioneers of American shock tubes was Walker Bleakney. Bleakney was a physicist who constructed the first Princeton shock tube in 1949 [15]. He performed studies on the formation of shock waves and their interactions with structures [16, 17]. Other scientists across the nation also performed shock-tube work, including Raymond Emrich at Lehigh, Irvine Glass at Toronto, Otto Laporte at Michigan, Abraham Hertzberg at Cornell, and several others. Many of these workers focused their efforts on either the basic principles of shock waves or on the inherent phenomena of shock-tube experiments, such as shock attenuation [9]. One application of these efforts was the study of high-speed aerodynamics. In 1958, in the wake of rapid growth in shock-tube research, a Navy-sponsored project on supersonic aerodynamics included a 600-page section on shock tubes [18].

In recent years, there have been several noteworthy advancements in the field of shock tubes. One area of advancement is in that of simulation. The current standard for shock-tube kinetics modeling is to assume a constant-volume reactor in the region behind the reflected shock. This is not completely accurate but has been used with satisfactory results for many years. However, attempts to model non-ideal effects behind the reflected shock have met with fairly good success in better describing experimental

data [8]. Another area of advancement has been increasing test times. Increasing test times is desirable if lower test temperatures are of interest. In order to accomplish this, extended driver sections and tailored driver gases have been employed. These techniques have allowed for test times as long as 35 ms or longer. This longer test time also allows for the study of the negative temperature coefficient regime [8]. A third area of improvement has been in the creation of more-uniform conditions behind the reflected shock. While the ideal shock tube would involve completely uniform conditions behind the reflected shock, this is not the case in reality. Instead, there is a gradual increase in pressure and temperature that occurs after the passage of the reflected shock. Even a small temperature rise (10 K) can have significant effects on the calculations of rate coefficients. Thus, this increase must either be mitigated or accounted for. The use of driver section inserts has been found to mitigate this problem. Rounded cones have been placed in the driver side and serve to reduce the pressure variations. Another solution to this problem has been the insertion of a buffer gas adjacent to the diaphragm in the driven section [8].

Shock tubes are devices that produce shock waves within gaseous mixtures. They consist of a driver side and a driven side. The driver side contains a gas (called the driver gas) at high pressure. The driven side contains gases (called the driven gases) at a much lower pressure. In between the two sections there is a breakable diaphragm. When the pressure differential between the two sections reaches some maximum value (determined by the thickness and material of the diaphragm), the diaphragm bursts open. The sudden change in pressure causes expansion waves to propagate into the driver

section and for a shock wave (the incident shock wave) to propagate into the driven section.

The passage of a shock wave causes a nearly instantaneous increase in both temperature and pressure behind the shock wave, and this occurs as the incident shock travels down the driven section. When the incident shock strikes the endwall of the shock tube, it is reflected back toward the driver side. At this point, the gas through which the reflected shock is traveling has already been heated and compressed. Due to the passage of the reflected shock, the driven gas is once again heated and compressed, this time to a greater extreme. The reflected shock has the additional advantage of serving to "freeze" the flow, that is, it reverses the flow that was induced by the passage of the incident shock and ideally brings the bulk velocity of the molecules to zero.

If the diaphragm breaks correctly, the shock wave produced is a normal shock. This means that the famous normal-shock relations can be used to calculate the conditions behind both the incident and reflected shocks [14]. Modern methods use computer codes to account for factors such as changes in specific heats. The codes output the temperature and pressure behind the reflected shock wave, which are the two parameters of highest interest. In order to calculate these parameters, several values must be known: the initial driven gas pressure, the properties of the driven and driver gases, and the velocity of the incident shock wave.

The initial driven gas pressure is measured by simple use of a pressure transducer prior to the bursting of the diaphragm. The properties of the driven and driver gases can be readily calculated by assuming ideal-gas mixtures. Measuring the velocity of the

incident shock wave presents the largest challenge. In modern experiments, this is typically done by placing high-speed (10-100 MHz bandwidth) pressure transducers along the length of the driven section and monitoring the pressure spike at each transducer as a surrogate for the time when the incident shock wave passes. If the difference in time of passage for each transducer is known and the distance between each transducer is known, then the average velocity of the wave between two transducers can be calculated.

Since the shock wave attenuates over the length of the tube, the velocity measurements are usually made at several different locations in order to estimate the attenuation, which is typically quite linear. The velocity of the incident shock can then be extrapolated out to the correct distance from the last measurement so that the true velocity at the endwall can be entered into the computer code. This code then yields the conditions behind the reflected shock wave, most importantly the pressure [atm] and temperature [K], P_5 and T_5.

Laser Diagnostics

One of the first uses of a shock tube to perform chemical kinetics studies was performed as a collaboration between Cornell and Los Alamos National Laboratory by Bauer and Schott in 1958. They utilized UV absorption spectroscopy of the OH molecule to study the decomposition of water behind the reflected shock [19]. This work

was built upon by work at CalTech, in which Lapp used a shock tube to measure some of the fundamental spectroscopic parameters of the OH molecule [20].

Ronald Hanson at Stanford has been one of the foremost pioneers of laser diagnostics for species concentration measurements. After working for some time with shock tubes and chemical kinetics, he published a paper in 1976 titled "Absorption of CO laser radiation by NO." In this work, he used a shock tube to heat a known amount of NO and to measure the spectroscopic parameters of NO based on the change in absorption of a CO laser [21]. This seminal work opened the door for a whole host of applications combining laser diagnostics with shock tubes. Of particular interest was the potential for making species-time-history measurements after the reflected shock in order to validate reaction rates. The next few years saw a flurry of related studies, involving spectroscopic studies [22], chemical kinetics studies [23], and even laser-based temperature measurements [24].

In recent decades, numerous developments have been made in the field of laser diagnostics. One such example was the development of planar laser-induced fluorescence (PLIF), which allows for a sheet of laser light to be shone through some reacting flow. A species of interest absorbs light at the particular frequency of the laser, but then fluoresces light at a different frequency. This light is recorded by a camera of some sort, and knowledge of the spatially varying concentration of the species of interest can be obtained [25]. Another development was the extension of tunable ring-dye lasers into the UV range using intra-cavity frequency doubling. This greatly enhanced the

number of molecules that could be accessed and thus opened the door for numerous other studies [26].

Laser absorption spectroscopy has been used extensively to study the H_2O molecule. One of the first examples appears to be the measurement of H_2O line parameters in the 10-micron region using a CO laser in 1978 [27]. One of the first studies using a laser to study H_2O behind reflected shock waves was performed by Salimian and Hanson in 1983. They utilized a CO laser at 5.26 microns to study spectroscopic parameters of H_2O from 1300 to 2300 K [28]. In 1987, Webster and May of CalTech used a suite of 8 tunable diode lasers (TDLs) to make simultaneous atmospheric measurements of H_2O, NO, and NO_2, among other molecules [29]. Nagali et al. performed measurements of Ar-broadened H_2O parameters near 1.4 microns [30]. TDLs have also been developed as temperature sensors in various applications [31, 32]. In recent years, Hong et al. have performed multiple studies of H_2O kinetic profiles behind reflected shock waves using TDL absorption; these studies are discussed in the following section [33-35].

The H_2/O_2 System

In the past several decades much effort has been spent on developing chemical kinetics mechanisms that contain details on hundreds of reactions. Examples of such mechanisms include the GRI Mech 3.0 and the AramcoMech 1.1. The GRI Mech is a compilation of 325 reactions that involves 53 species, while the AramcoMech is a

compilation of 1287 reactions that involves 188 species [6, 7]. The reaction rates for each of these reactions must be included in the mechanism. Some of these are calculated with theory while others are measured experimentally. Therefore, contributors to chemical kinetics spend much time measuring elementary reaction rates to further develop these mechanisms. Tools such as flow reactors and shock tubes have been used to do this. Common techniques used in shock tubes include emission and laser absorption spectroscopy in both the IR and the UV.

The H_2/O_2 system is a key component of any hydrocarbon combustion mechanism because all higher-order hydrocarbons eventually reach some level of H_2/O_2 reaction. Also, the H_2/O_2 mechanism contains many elementary reactions involving H, O, OH, HO_2, and several other radicals that play an important role in every hydrocarbon reaction [1]. As such, a considerable amount of work has gone into developing accurate kinetics mechanisms to describe this reaction set. The GRI Mech contains 20 elementary reactions in its H_2/O_2 sub-mechanism [6]. Several other H_2/O_2 mechanisms have been published since the GRI Mech by Li et al., Ó Conaire et al., and Konnov [3-5].

Despite the vast importance of the H_2/O_2 system and the work that has been put into it, questions still remain about the accuracy of the rate coefficients for quite a few of the reactions. Reactions that have been closely scrutinized include reactions between H atoms and HO_2 radicals and the pressure dependence of HO_2 recombination, among others. Konnov investigated the prudence of eliminating the reaction $H+HO_2 = H_2O + O$ based on its kinetic similarity to the reaction $H+HO_2 = OH + OH$, which was a simplification that both Li et al. [4] and Ó Conaire et al. [5] employed in their

mechanisms. Konnov suggests in his work that these reactions cannot be assumed to be similar under all conditions based on the opposite signs of their sensitivities. Konnov also mentions that the low-pressure regime of the previous two mechanisms were not supported by experimental data [3].

In another attempt to answer these questions, more data on these elementary reactions were acquired between 2008 and 2011 by Hong et al. from the Hanson group [33-35]. They utilized UV and IR laser absorption spectroscopy behind reflected shock waves to infer several key reaction rates. The wavelengths employed were near 300 nm (for the OH molecule) and near 2.5 μm (for the H_2O molecule). Using these new experimental data and others, Hong et al. released a new version of the H_2/O_2 mechanism in 2011. This mechanism contains the same 20 elementary reactions from the GRI Mech 3.0, though only five of the original reaction rates are retained. The new mechanism shows excellent agreement with the experimental data [2].

The Hanson group is currently the only group of investigators known to the author that is actively employing laser absorption spectroscopy in a shock tube to study the H_2/O_2 system. This research group has an extremely long and prestigious track record. It would be beneficial, however, to have collaborative data with which to back up their results and to perhaps answer some of the remaining questions about the H_2/O_2 system.

Quantum Mechanics

The field of quantum mechanics is relatively new in the context of world history. Prior to the 20th century, it was non-existent. However, the early 1900's saw a flurry of discoveries in this area, due to the work of Eisntein, deBroglie, Heisenberg, Planck, and many others. Their combined work led to the discovery of the astounding fact that molecules do not exist across a continuum of energy states but rather at discrete energy levels. Furthermore, molecules change spontaneously from one energy state to another, and the rate at which specific changes occur can be predicted by statistical methods.

Molecules possess several different modes of storing energy. In absorption spectroscopy, the modes are typically limited to translational, rotational, vibrational, and electronic. The translational mode of energy storage is insignificant compared to the other three and is thus neglected. Therefore, the discrete energy states noted above can be classified as either rotational, vibrational, or electronic, and as noted previously, molecules spontaneously move between these states. Due to the interaction of light and matter, molecules absorb and emit light that has energy corresponding to the difference between these levels. The well-known Planck equation relates a photon's energy E [J] and its frequency v [Hz] by Planck's constant h [J s], or

$$E = hv \tag{1}$$

Since absorption spectroscopy centers on measuring the *difference* between energy states, it is helpful to recast (1) as

$$\Delta E = E_2 - E_1 = h\nu_{2,1} \tag{2}$$

In this equation, ΔE is the difference between two energy states, say E_2 and E_1. Thus, $\nu_{2,1}$ is the frequency of the light that would be either emitted or absorbed by a molecule that is *transitioning* between these two energy states. However, the groundbreaking theorem of quantum mechanics postulates that these energy states are discrete rather than continuous. Thus, by introducing ϵ_j as discrete energy states [J] at which molecules can exist, (2) can be rewritten as

$$\epsilon_{j+1} - \epsilon_j = h\nu_{j+1,j} \tag{3}$$

Equation (3) relates the difference between energy states ϵ_{j+1} and ϵ_j to the frequency $\nu_{j+1,j}$ of the light emitted or absorbed by this transition. This line of thinking gives rise to calling a change between specific energy states "the transition at $\nu_{j+1,j}$", where $\nu_{j+1,j}$ is an actual numerical value of frequency. The wavelength λ [m] of a transition can also be used in place of frequency, and is related to frequency by

$$\lambda = \frac{c}{v} \tag{4}$$

The constant c is the speed of light [m s^{-1}]. Spectroscopists often prefer wavenumber over wavelength or frequency. Wavenumber $\bar{v}$ has units of inverse distance, typically [cm^{-1}], and is given by

$$\bar{v} = \frac{1}{\lambda} \tag{5}$$

One concept that is utilized in a later section is that of the partition function. The total partition function Q is defined as

$$Q = Q_{rot}\, Q_{vib}\, Q_{elec} \tag{6}$$

In this equation, Q_{rot}, Q_{vib}, and Q_{elec} are the rotational, vibrational, and electronic partition functions. The partition function itself is a difficult concept to understand, and there are many different methods used to define it. One such method is the mathematical definition, which states that

$$Q_{()} = \sum_j\ g_j\ exp\left(-\frac{\epsilon_j}{kT}\right) \tag{5}$$

Here, g_j is the degeneracy of the j^{th} indexed level, k is Boltzmann's constant [J K^{-1} $molecule^{-1}$], and T is the temperature [K]. Note that $Q_{()}$ is used to denote any of the previously mentioned partition functions. It can be seen from this expression that a higher temperature results in a larger value of $Q_{()}$. Conceptually, the partition function can be thought of as a way to quantify how molecules in a substance are distributed throughout the available energy levels. The larger value of $Q_{()}$ at higher temperatures represents that the higher energy levels are more populated than they would be at lower temperatures.

CHAPTER III

DESCRIPTION OF THE LASER DIAGNOSTIC

Spectral Modeling

The fundamental relation of absorption spectroscopy is the Beer-Lambert law, which relates the transmitted and incident light intensities, I and I_0 [W m^{-2}], of monochromatic light passing through a weakly absorbing medium by

$$\frac{I}{I_0} = \exp(-P_{tot} X_{abs} L\, k_v) \tag{7}$$

In this equation, P_{tot} is the total pressure of the medium [atm], X_{abs} is the mole fraction of the absorbing species, L is the path length through the medium [cm], and k_v is the spectral absorption coefficient [cm^{-1} atm^{-1}]. Often, k_v is simply referred to as the absorption coefficient. In species time-history measurements, X_{abs} is the quantity that is sought. The transmittance $\frac{I}{I_0}$ and the total pressure are measured experimentally, and the path length is easily obtainable.

The absorption coefficient, however, requires special attention. It is given by

$$k_v = S(T)\, \phi(\bar{v} - \bar{v}_0) \tag{8}$$

The first term in (8), $S(T)$, is the line strength [cm^{-2} atm^{-1}] and is only a function of temperature. The line strength of a transition with line center at $\bar{\nu}_0$ [cm^{-1}] can be described as a function of temperature by

$$S(T) = S(T_0)\frac{Q(T)}{Q(T_0)}\left(\frac{T_0}{T}\right)\exp\left[-\frac{hcE''}{k}\left(\frac{1}{T}-\frac{1}{T_0}\right)\right] \times \left[1-\exp\left(-\frac{hc\bar{\nu}_0}{kT}\right)\right]\left[1-\exp\left(-\frac{hc\bar{\nu}_0}{kT_0}\right)\right]^{-1} \quad (9)$$

Here, T_0 is a reference temperature [K] and E'' is the lower-state energy, typically in [cm^{-1} molecule^{-1}]. Note that if c is in [m s^{-1}] and E'' is in [cm^{-1} molecule^{-1}], care must be taken with unit conversions [36].

Mathematical or semi-empirical expressions have been obtained for Q_{rot}, Q_{vib}, and Q_{elec} so that Q can be completely evaluated. However, evaluating these expressions can be tedious. One way to circumvent this issue is to use fitting polynomials that estimate the partition function. Numerous databases have been compiled to make this information readily available. One example is the High Resolution Transmission (HITRAN) database. This database contains detailed spectral information on a total of 39 molecules, including the location of transitions, line strengths, and broadening parameters, among others. This database can be used in conjunction with the Java HITRAN Atmospheric Workstation (JavaHAWKS) program. This program accesses the HITRAN 2004 database and extracts desired spectral data from it. Of key interest is the fact that JavaHAWKS uses the database information on the partition function to calculate the line strength of various transitions at a specified temperature. In this way,

the use of (9) can be avoided, thereby simplifying the calculation of the absorption coefficient. For more information on HITRAN and JavaHAWKS, see [37, 38].

The second term in (8), $\phi(\bar{\nu} - \bar{\nu}_0)$, is the line shape function [cm], where $\bar{\nu}$ [cm^{-1}] is a range of wavenumbers centered around $\bar{\nu}_0$. The line shape function quantifies the spread around a transition. Though transitions from one energy state to another do occur at discrete frequencies, there are effects that cause molecules to absorb and emit at slightly different frequencies than the actual line center. These effects are called broadening effects because they serve to broaden the discrete frequencies at which molecules absorb and emit into wider ranges of frequencies. Broadening effects are generally placed into three categories: Heisenberg broadening, thermal broadening, and collisional broadening.

Heisenberg broadening refers to the natural broadening of spectral lines due to the Heisenberg Uncertainty Principle. The principle states that on a microscopic scale, it is impossible to simultaneously measure both velocity and position. In this present work, the contribution of Heisenberg broadening relative to the other two types of broadening is minimal, and thus it is neglected.

Thermal broadening, or Doppler broadening, is a result of the fact that a group of molecules in a fixed volume at a uniform temperature actually travel through the volume at varying velocities. The distribution of these velocities is described by the Maxwellian velocity distribution. A fixed observer will appear to see some molecules traveling faster and others slower due to this distribution. In a manner similar to the acoustic Doppler

Effect, these differing relative velocities cause some of the light that is absorbed or emitted by the molecules to shift in frequency.

Collisional broadening is a result of the fact that molecules collide with one another. These collisions transfer energy, and thus reduce the likelihood that molecules remain at a particular energy level for a long period of time. This collisional transfer increases the uncertainty as to the exact energy level of molecules, hence serving to broaden a transition line. An important side note is that molecular collisions also serve to shift the center frequency of a spectral line in a phenomenon called collisional shifting.

When only thermal effects are important, a Gaussian profile is used to model the Doppler broadening. When only pressure effects are important, a Lorentzian profile is used to model the collisional broadening. When both effects are important, a Voigt profile is used to model the convolution of the two types of broadening. In combustion applications, both effects are typically important and thus a Voigt profile is used. The Voigt profile is described by Gharavi and Buckley [36] as

$$\phi(\bar{\nu} - \bar{\nu}_0) = AK(x, y) \tag{10}$$

$$A = \frac{1}{\gamma_D}\sqrt{\left(\frac{\ln(2)}{\pi}\right)} \tag{11}$$

$$K(x, y) = \frac{y}{\pi}\int_{-\infty}^{\infty} \exp\frac{(-t^2)}{y + (x - t)^2}\, dt \tag{12}$$

In (12), t is a variable of integration, while y and x are given by

$$y = \frac{\gamma_L}{\gamma_D}\sqrt{\ln(2)} \tag{13}$$

$$x = \left[\frac{\bar{\nu} - \bar{\nu}_0}{\gamma_D}\right] \tag{14}$$

Here, $\gamma_D$and $\gamma_L$are the half-widths at half-maximum (HWHM) of the Doppler and Lorentzian profiles [cm^{-1}]. The Doppler HWHM for a transition at $\bar{\nu}_0$ is well-known for a molecule with molecular mass M [kg kmol^{-1}] as

$$\gamma_D = 3.581 \times 10^{-7}\, \bar{\nu}_0 \sqrt{\frac{T}{M}} \tag{15}$$

The Lorentzian HWHM for collisional broadening is slightly more difficult to evaluate, or at least more empirical in nature. Rothman et al. [39] define $\gamma_L$as a function of temperature and pressure by

$$\gamma_L = \left(\frac{T_0}{T}\right)^n \left(\gamma_{air} P_{pert} + \gamma_{self} P_{abs}\right) \tag{16}$$

Here, n is the temperature exponent, γ_{air} [cm^{-1} atm^{-1}] is the air-broadened HWHM at reference pressure and temperature, γ_{self} [cm^{-1} atm^{-1}] is the self-broadened HWHM at

reference pressure and temperature, P_{pert} [atm] is the partial pressure of the perturbing species (which may or may not be air), and P_{abs} [atm] is the partial pressure of the absorbing species. HITRAN provides n, γ_{air}, and γ_{self} at reference conditions of 1 atm and 296 K. Note that it is seen from (16) that the temperature dependence of γ_{self} is assumed to be the same as that of γ_{air}. Also, since in these experiments the perturbing species is Ar rather than air, a correction factor must be applied to both n and γ_{air}. Nagali et al. give suggested correction factors of 1.0 for n and 0.4 for γ_{air} [30]. These values are used for this study; their validity is discussed later.

The integral in (12) is difficult to evaluate. Instead, various numerical techniques have been formulated as approximations. Whiting [40] gives the absorption cross-section σ_v [cm^2 molecule^{-1}] based on the Voigt profile as

$$\sigma_v(\nu) = \sigma_v(\nu_0)\left\{(1-a)\exp(-0.693b^2) + \frac{a}{1+b^2} + 0.016(1-a)a \times \left[\exp(-0.0841b^{2.25}) - \frac{1}{1+0.0210b^{2.25}}\right]\right\} \quad (17)$$

$$a = \frac{\gamma_L}{\gamma_V} \quad (18)$$

$$b = \frac{|\bar{\nu} - \bar{\nu}_0 - \delta P|}{\gamma_V} \quad (19)$$

HITRAN gives the collisional shift parameter δ [cm^{-1} atm^{-1}] from (19) at reference conditions of 1 atm and 296 K, while P is the total pressure [atm] of the system. The

collisional shift term is not present in the original equations from Gharavi and Buckley but has been added here for thoroughness. The γ_V term in (18) and (19) is the Voigt profile HWHM [cm^{-1}] and is given by

$$\gamma_V = 0.5346\gamma_L + (0.216\gamma_L^2 + \gamma_D^2)^{0.5} \tag{20}$$

The $\sigma_\nu(\nu_0)$ term in (17) is the absorption cross-section at line center [cm^2 $molecule^{-1}$] and is given by

$$\sigma_\nu(\nu_0) = \frac{S(T)}{2\gamma_V(1.065 + 0.447a + 0.058a^2)} \tag{21}$$

The preceding equations can be used to calculate the Voigt profile. A comparison of the Gaussian, Lorentzian, and Voigt profiles is shown in Figure 1. This figure demonstrates how thermal and collisional broadening move the absorption away from the line center. Note how the Voigt profile closely resembles the Lorentzian profile in the outskirts of the figure.

Equation (17) gives the absorption cross-section σ_ν, which is in [cm^2 $molecule^{-1}$]. However, the desired quantity is the absorption coefficient k_ν, which has units of [$cm^{-1}atm^{-1}$]. Clearly, some kind of unit conversion is necessary. The Loschmidt constant N_L^0 gives the number of ideal gas molecules in a fixed volume at standard conditions. At 296 K and 1 atm, it is given as 2.48×10^{19} [molecules cm^{-3} atm^{-1}]. By the ideal gas law,

the conversion of N_L^0 to a different temperature and the absorption coefficient k_v are given by

$$N_L = N_L^0 \left(\frac{T_0}{T}\right) \tag{22}$$

$$k_v = \sigma_v N_L \tag{23}$$

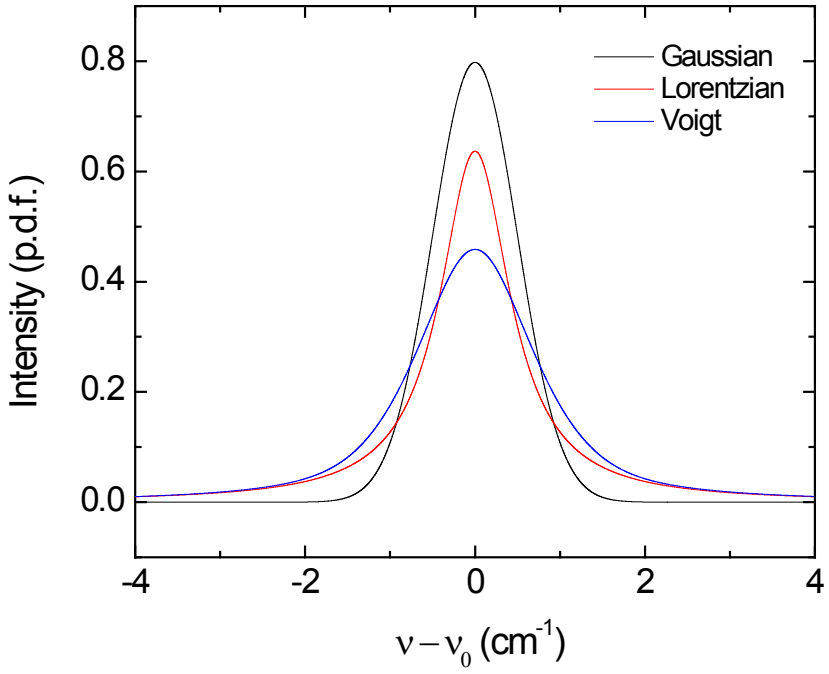

Figure 1. Comparison of Gaussian, Lorentzian, and Voigt profiles. Calculations are made with HWHM values of 0.5 cm^{-1} for both the Gaussian and Lorentzian profiles. The Voigt profile is estimated by the expression from Whiting [40].

Experimental Setup

A schematic of the experimental setup is shown in Figure 2. A Toptica Photonics DL-100 TDL is used to produce coherent laser light. The laser is controlled using a Toptica Photonics DC 110 diode laser controller. This controller allows for precise control of both the temperature of the laser diode and the current flowing through the diode. The light leaving the laser is split using a 90/10 beamsplitter. The 10% beam is directed into a Burleigh WA-1000 wavemeter to allow for real-time monitoring of the laser wavelength. Control of the laser temperature and current allows for precise selection of this wavelength. The 90% beam is passed into a 50/50 beamsplitter. One of the resulting beams is directed into a Newport Corporation 2317NF large-area balanced photoreceiver to monitor the incident intensity, I_0. This detector has a maximum bandwidth of 150 kHz, which is typically a bit slow for shock-tube experimentation. However, H_2O kinetics are relatively slow, so this time-response proved adequate. The other beam is passed through the shock tube window ports and then into another 2317NF detector to monitor the transmitted intensity, I.

The voltage signals from the sidewall pressure transducer and the two photoreceivers are monitored by a PC with a GageScope high-speed digitizer that samples at 1 MHz. Before the photoreceiver signals are sent to the PC, they pass through a Stanford Research Systems model 560 differential preamplifier. This preamplifier subtracts the two signals, thus outputting one signal that is I_0 and another that is $I_0 - I$. This method, known as common mode rejection, allows for common noise in the two

signals to be eliminated. It also has the benefit of allowing the full-scale range in GageScope to be minimized, thus reducing the bit noise. This reduction in bit noise plays a noticeable role in reducing the overall noise in the signal.

Two sealed boxes made of sheets of Lexan are used to minimize beam attenuation due to ambient water vapor. These boxes individually enclose both the incident and transmitted sides of the laser diagnostic, though small leaks are intentionally left in both boxes. N_2 is flooded into the enclosures so that the ambient water vapor is forced out through the small leaks. The relative humidity within the boxes is monitored using an Omega Engineering RH85 handheld hygrometer. A relative humidity of less than 0.1% is maintained for all shock-tube runs. To minimize beam attenuation, the laser is situated very near the first Lexan enclosure so that the beam need only pass through a small amount of ambient water vapor.

Proper optical techniques are used in an attempt to ensure minimum noise from beam steering and other such effects. All optics are firmly tightened and clamped down. An iris is placed immediately in front of each photoreceiver to reduce the amount of stray light striking the photoreceiver. Each iris is reduced to a diameter of about 2 mm. The beam diameter is difficult to ascertain with a viewing card, but it is estimated to be about 1.5 mm before passing through any focusing optics. A bandpass filter is also placed directly in front of each photoreceiver. Each filter is centered at 1384 nm and has a full-width at half-maximum of 20 nm. A plano-convex CaF_2 focusing lens with a focal length of 10 cm is placed in front of each photoreceiver. It is known that plano-convex lenses are less sensitive to vibrations when the plane surface is facing the focal point; the

lens on the transmitted side is thus situated in this manner. See Figure 3 for a photo of the optical setup and shock tube.

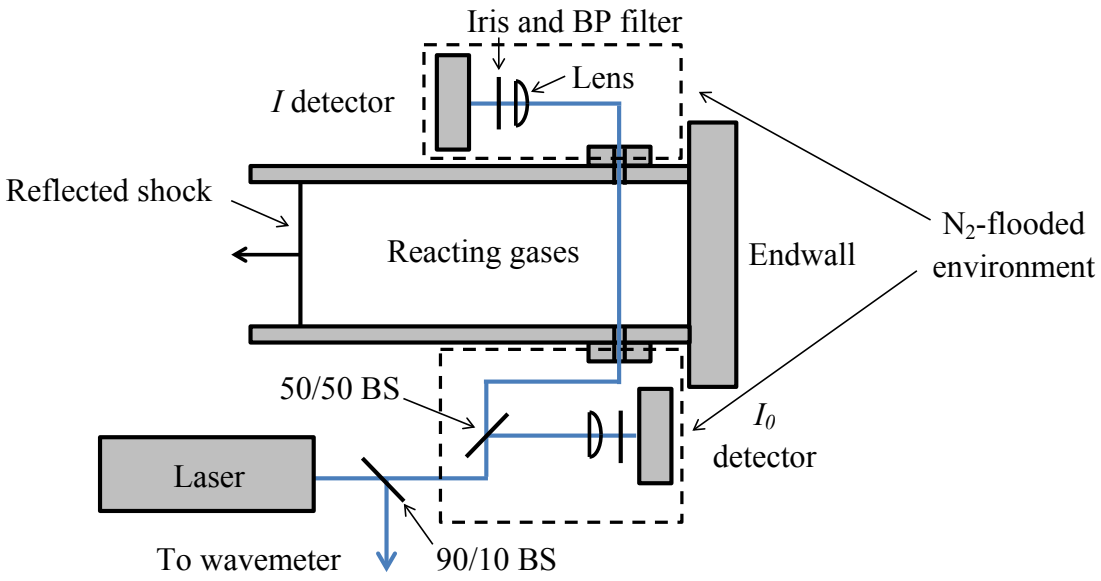

Figure 2. Schematic of the experimental setup. Not shown is the tubing used to constantly flood the Lexan boxes with N_2.

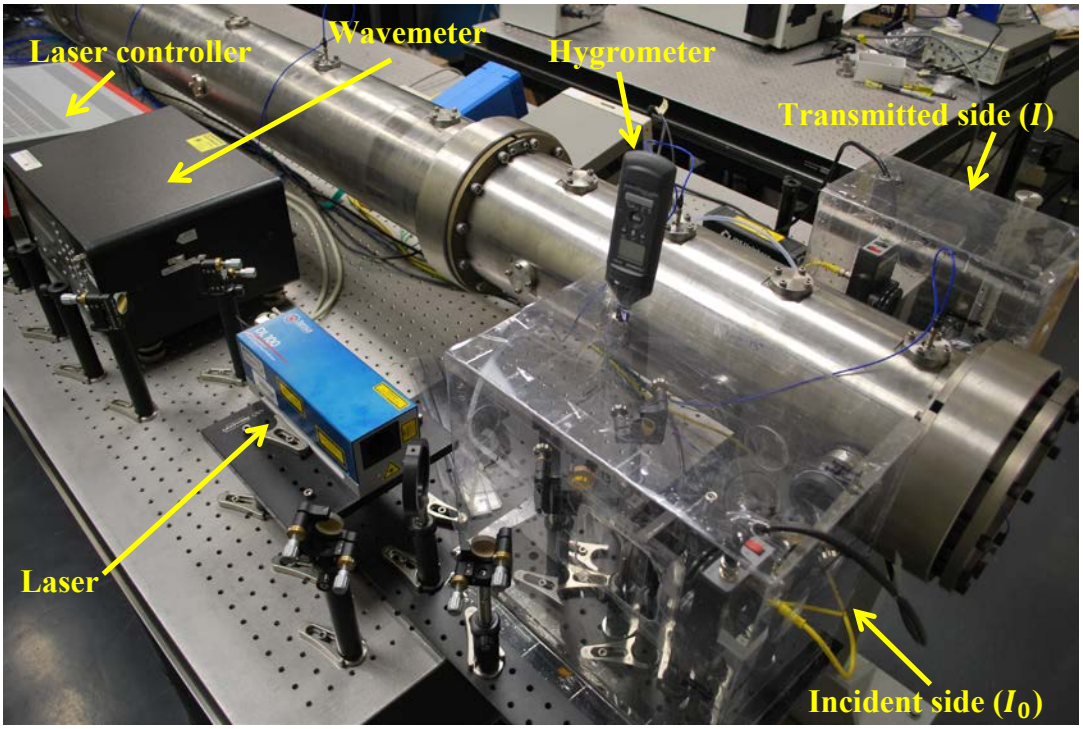

Figure 3. Picture of the laser setup for this study. Note the proximity of the laser to the Lexan enclosure. Also note that the shock tube is vibrationally isolated from the optics.

The laser has a usable power output at wavelengths from 1380 to 1392 nm. At the experimental conditions of this study, the transition at 1388.139 nm is the strongest transition available. Thus, the laser is tuned to this wavelength for all experiments. This wavelength is relatively steady, showing little tendency to mode hop to other wavelengths. A demonstration of the varying line strengths in the usable wavelength range of the laser is shown in Figure 4.

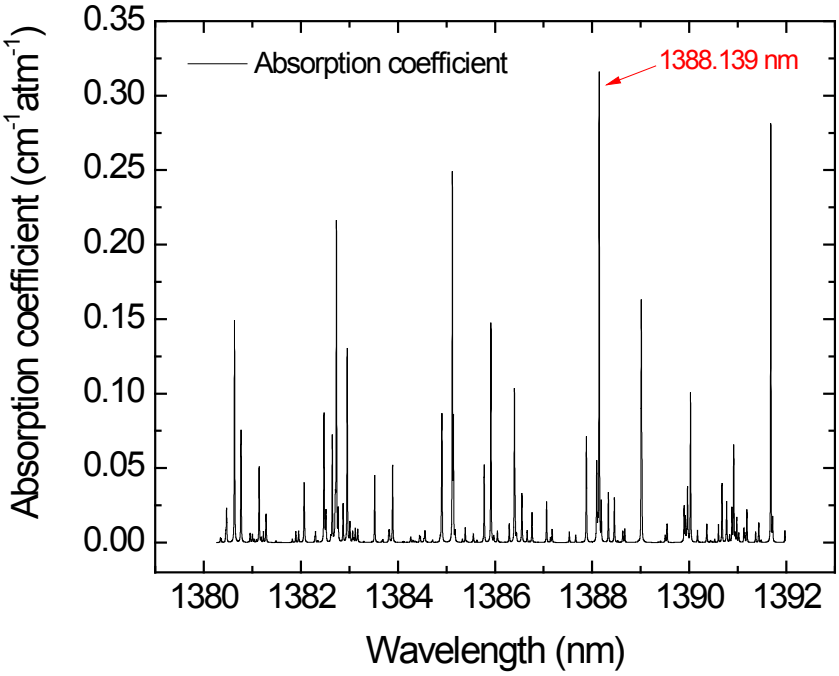

Figure 4. Variation of the absorption coefficient with wavelength. Results are calculated at 1300 K, 2.7 atm in 0.6% H_2O, 99% Ar.

A schematic of the shock tube used in these experiments is shown in Figure 5. This shock tube was donated from the Aerospace Corporation and has now been retrofitted for use at Texas A&M University. The driver section has a length of 3 meters and the driven section has a length of 6.78 meters. The driven section has an inner diameter of 16.2 cm and a wall thickness of 1.27 cm. The inner surface of the driven section has a surface finish of 1 micron RMS or better to reduce boundary layer growth. Several options are available for diagnostic access to the shock tube. The last two sections of the shock tube have a total of 28 sidewall ports. The endwall section of the

shock tube has a total of five endwall ports. These 33 ports offer access to the tube and are typically used to make either pressure measurements or optical measurements.

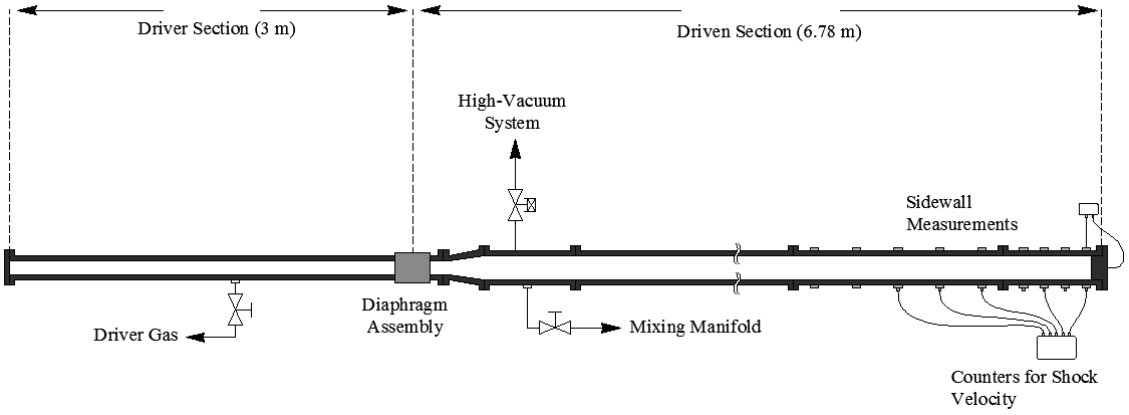

Figure 5. Schematic of the shock tube [41]. Note that though the endwall pressure is indicated in the schematic, it is not used in the present study.

Five PCB 113B22 fast-response, piezoelectric pressure transducers are used to measure the sudden pressure rise that marks the passage of the incident shock wave. The time intervals between consecutive pressure rises (a total of four intervals) are measured by four Fluke/Phillips PM6666 high-frequency time-interval timers. These measurements allow for calculation of both the shock velocity and the attenuation of the shock velocity. The intervals are measured over the last meter of the driven section and the measured attenuation of the shock velocity is used to extrapolate the shock velocity out to the endwall.

The sidewall pressure is measured through the use of a Kistler 601B1 high-sensitivity, charge-output pressure transducer. The sensor is located at a sidewall port 1.6 cm from the endwall. In dilute mixtures such as the ones used in this study, minimal pressure rise is expected during the test time, but this expectation can be validated through sidewall pressure measurements. Located in the same axial plane as the sidewall pressure transducer are two sapphire window ports. Sapphire has a transmissivity of about 80% in the near-IR and is thus useful for these laser measurements.

Mixtures for experiments are prepared in a separate mixing tank. This tank is vacuumed to a pressure of $<10^{-5}$ torr prior to each mixture being prepared. The constituents are added manometrically using two MKS Baratron capacitance manometers model 626B (0-10 torr and 0-1000 torr) and one Setra pressure transducer model 225 (0-250 psia). For a thorough description of the shock-tube facility, see the thesis by Vivanco [41].

CHAPTER IV

RESULTS AND DISCUSSION

H_2O Time-Histories

H_2O time-histories were obtained over the course of the shock-tube test time. Shown herein are the results for one experiment; the full results can be found in the Appendix. Figure 6 shows a representative sidewall pressure trace from a shock-tube experiment. Several features can be noted from this figure. The first rise in pressure marks the passage of the incident shock. The second rise marks both the passage of the reflected shock and the beginning of the experiment. The decrease in pressure that occurs at about 2500 microseconds marks the end of the experiment. This decrease is due to the arrival of the expansion wave that has reflected off the far end of the shock tube and made its way to the endwall.

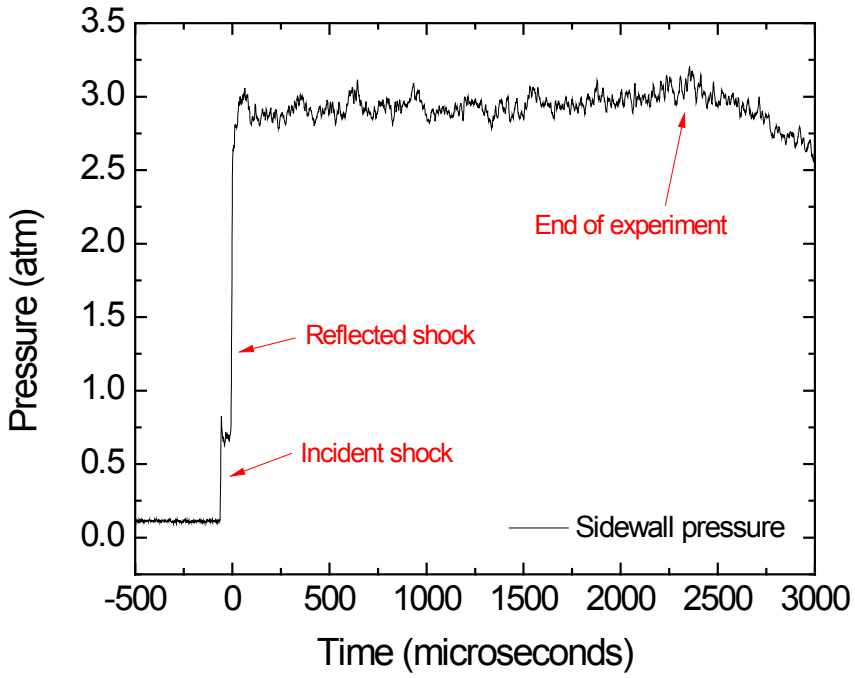

Figure 6. Representative sidewall pressure trace. Note the minimal pressure rise during the course of the experiment. Results are at 1402 K, 2.877 atm in 0.33% O_2, 0.66% H_2, balance Ar.

A sample H_2O time-history is shown in Figure 7. The general shape of the profile matches well with what the literature predicts; more discussion is given on this topic later. The large spike at time 0 does not actually represent any H_2O formation; it is rather an artifact of shock-tube experiments. The term for this phenomenon is a Schlieren spike, and it is caused by the large density gradient that exists across the reflected shock wave. The peak of this wave marks the beginning of the high-temperature and -pressure conditions behind the reflected shock wave, and thus it is set to be time 0 for the experiment; this time corresponds precisely to the second pressure rise seen in the

sidewall pressure trace. Another item to note is the level of noise in the signal. The data represent an uncertainty in H_2O concentration of ±200 ppm, which represents ±3% noise. This level of noise is acceptable though not exemplary. However, an inspection of the raw signal from the photodetectors reveals that the current level of noise is actually quite good. The inherent laser/detector noise prior to the incident shock wave is ±1.5 mV. Since the I_0 signal level is about 1.89 V, this corresponds to ±0.08% noise. During the actual experiment, the noise level is a bit higher at ±3 mV, but this is still only a noise level of ±0.16%. The reason for the order of magnitude increase in noise between the raw signal and the calculated concentration is the low amount of absorption at these conditions. The amount of water present in these mixtures is quite low, and thus the total absorption is only 3.8%.

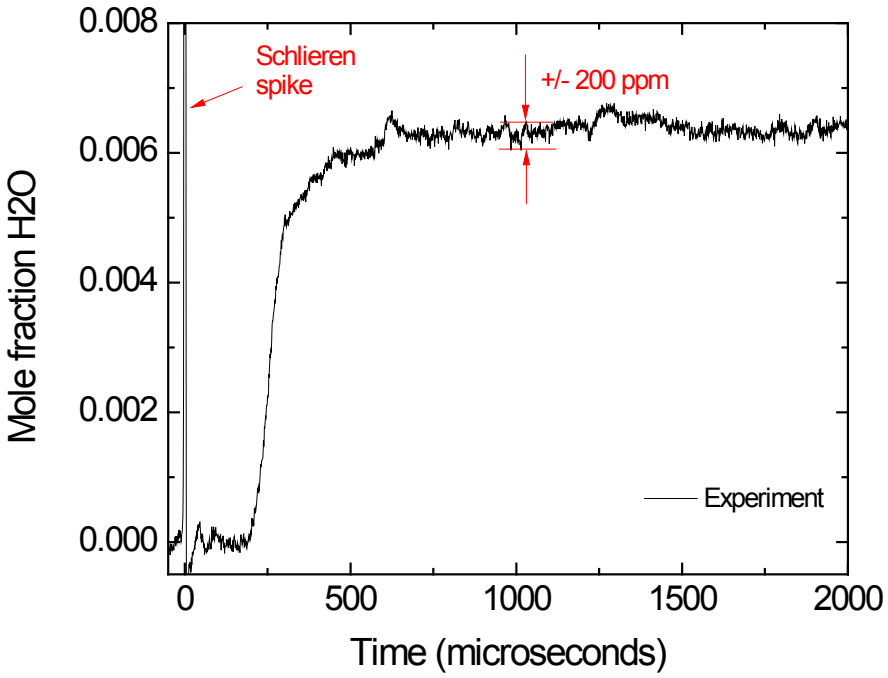

Figure 7. Representative H_2O time-history. Note the second Schlieren spike from the reflected shock; the first spike from the incident shock is not shown. Results are at 1402 K, 2.877 atm in 0.33% O_2, 0.66% H_2, balance Ar.

The experimental data are compared with the mechanism from Hong et al. [2] in Figure 8. While the general shape seems to agree somewhat well, there is a noticeable discrepancy in terms of the amount of H_2O actually formed. This discrepancy can be attributed to errors in the spectroscopy used to calculate the absorption coefficient. This error is discussed in more detail later. Another feature that is worth noting is the ignition delay time. The model and the data are in fair agreement; ignition delay times are discussed in more detail in a later section.

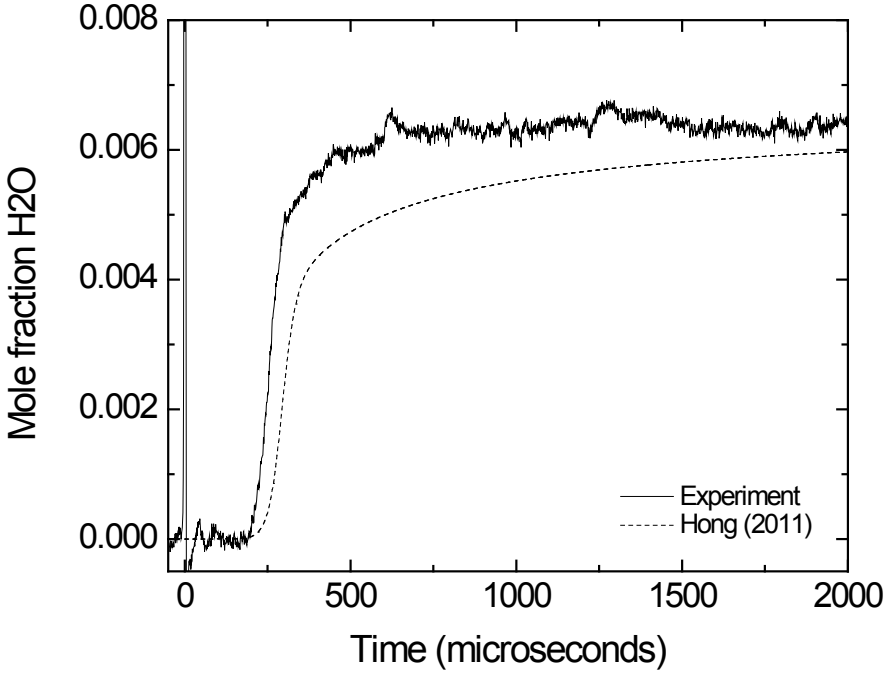

Figure 8. Comparison of the experimental data to the model from Hong. A constant absorption coefficient is used to calculate the mole fraction of H_2O. Results are at 1402 K, 2.877 atm in 0.33% O_2, 0.66% H_2, balance Ar.

It is worth noting here that the equilibrium chemistry of H_2O is well-studied. While the kinetics of H_2O are not necessarily known and are hence being investigated here, the equilibrium mole fraction of H_2O can be calculated very accurately. Whether or not the Hong mechanism accurately predicts the kinetics of H_2O remains to be seen, but the equilibrium values are predicted with extreme accuracy. It is not possible for the mixture to exceed the equilibrium value of H_2O and thus it seems appropriate to rescale the experimental data by changing the absorption coefficient. The results of this rescaling are shown in Figure 9. The mole fraction of H_2O at equilibrium, 0.00668, is

displayed on the graph. It is seen that the transient H_2O profile is approaching this equilibrium value, as is expected.

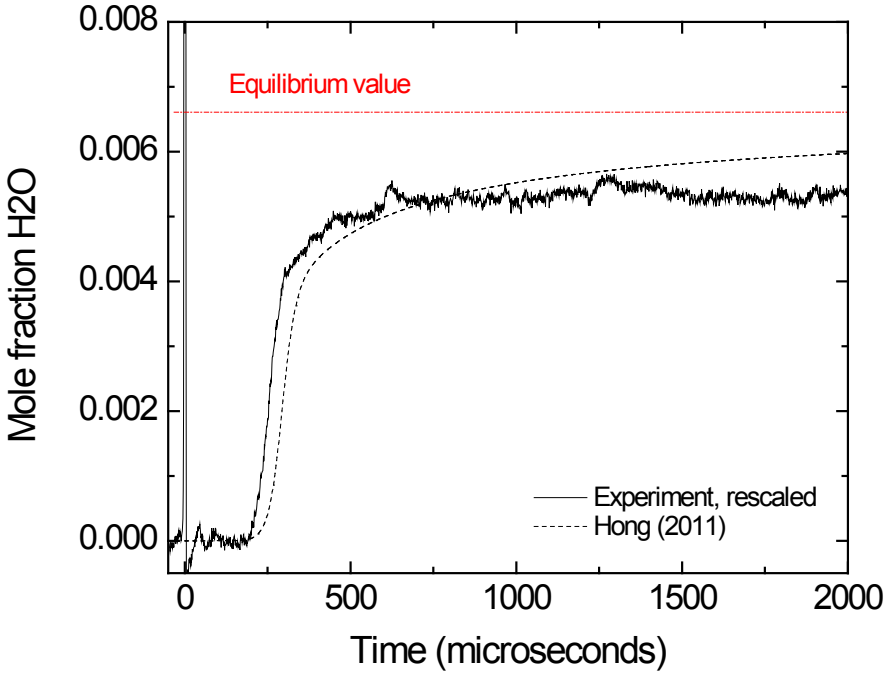

Figure 9. Comparison of rescaled data to the Hong mechanism. Note the difference in shape at the tail end of the profile. The equilibrium amount of H_2O is shown. Results are at 1402 K, 2.877 atm in 0.33% O_2, 0.66% H_2, balance Ar.

The rescaling of the absorption coefficient in Figure 9 reveals that the experimental data and the model differ noticeably in shape. The initial formation of H_2O agrees well with the model. However, the experimental profile seems to flatten out while the model continues to curve upwards as the experiment nears conclusion. This difference in shape can be explained by the temperature dependence of the absorption

coefficient. As discussed previously, both line strengths and spectral broadening parameters depend strongly on temperature. Therefore, if there is a change in temperature within the shock tube over the course of the experiment, there is a corresponding change in the absorption coefficient. This phenomenon is addressed in the following section.

Absorption Coefficient Correction

Highly dilute mixtures are preferred for kinetics studies because the temperature rise due to combustion is minimized. However, high dilution comes with the price of small amounts of absorbing species. Less absorbing species means less absorption, which decreases the signal-to-noise ratio (SNR). Thus, a trade-off must be made between these competing factors. The mixture used in this study was a stoichiometric mixture of H_2/O_2 diluted in 99% Ar. This mixture was chosen because it allowed for reasonable signal levels while keeping the temperature rise at a manageable level.

However, the average temperature rise for this mixture is still 100 K, as simulated by the CHEMKIN software suite using the Hong mechanism. It is found that the change in absorption coefficient due to this temperature rise is quite significant; a reduction of about 30% is typical. A custom MATLAB routine is used to correct for this change in temperature coefficient. This routine utilizes the simulated results for temperature, pressure, and H_2O concentration and recalculates the absorption coefficient at intervals of one microsecond across the entire test time. The corrected absorption

coefficient and the simulated temperature are both plotted versus time in Figure 10. The absorption coefficient decreases from 0.113 to 0.088 $cm^{-1}atm^{-1}$ over the course of the experiment. Note that the discontinuities in the corrected absorption coefficient curve are not truly present, but are simply a result of the rounding used when evaluating the line strengths from JavaHAWKS.

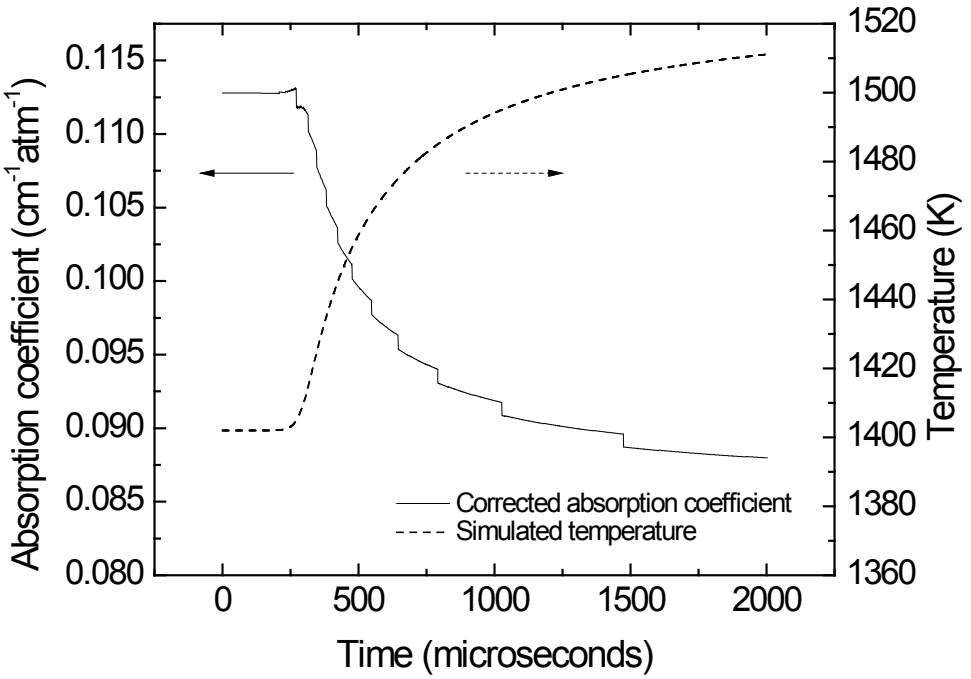

Figure 10. Corrected absorption coefficient and simulated temperature. The discontinuities are a product of the rounding used in the calculations. Calculations are at 1402 K, 2.877 atm in 0.33% O_2, 0.66% H_2, balance Ar.

The absorption coefficient correction can be applied to the experimental data in an attempt to rectify the observed discrepancy in the shape of the profile. The results of

this correction are shown in Figure 11. It is evident that a large disagreement persists in terms of the amount of H_2O formed. However, it appears that the shapes of the two profiles are in much better agreement than before. Rescaling the experimental as before proves whether or not this is true. Figure 12 shows the results of this rescaling. It can be seen that the model and the experimental data are now in excellent agreement, with the tail ends of the two profiles aligning much more closely than before. One can thus conclude that the temperature rise explains the initial difference between data and model and that this difference can be remedied by correcting the absorption coefficient.

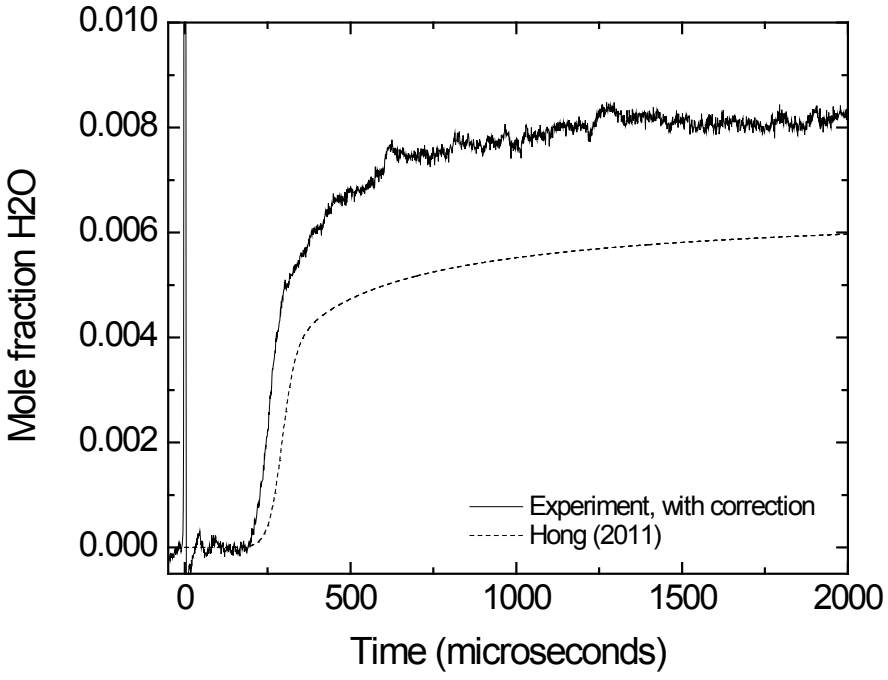

Figure 11. Model versus experimental data with absorption coefficient correction applied. Note the improved agreement in the shape of the profile. Results are at 1402 K, 2.877 atm in 0.33% O_2, 0.66% H_2, balance Ar.

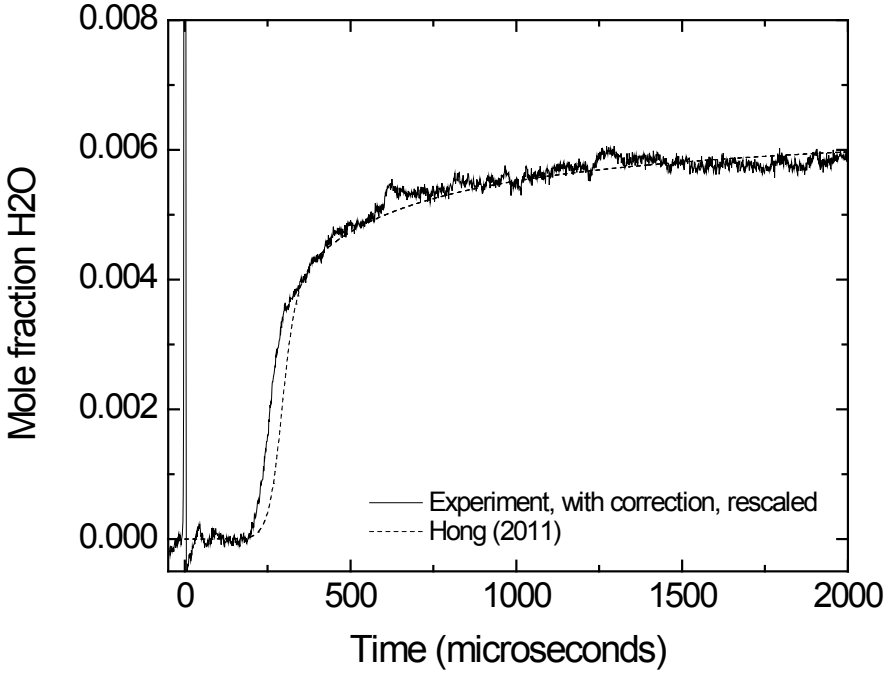

Figure 12. Model versus experimental data with absorption coefficient correction applied. The experimental data have also been rescaled to match the model. Excellent agreement is seen. Results are at 1402 K, 2.877 atm in 0.33% O_2, 0.66% H_2, balance Ar.

The need to rescale the absorption coefficient after correcting for the temperature change has several possible explanations. First is the possibility of an error in the calculations. The steps to calculate the absorption coefficient are quite involved, and the possibility of an error is not to be discounted. Comparisons of calculations have been made with other sources, but these calculations are made at ambient conditions rather than at elevated temperatures, and thus it is difficult to say for certain whether the calculations are accurate at shock-tube conditions.

A second possible explanation for inaccuracies in the absorption coefficient is the uncertainty of the wavemeter. The wavemeter display has a resolution of 0.001 nm, thus a reasonable accuracy to assume is ±0.0005 nm. The laser was tuned to 1388.139 nm for all experiments. As discussed previously, this wavelength was chosen because it was believed to be the line center of the transition at 1388.139 nm. However, it was realized during post-processing that this was not the case. Due to the collisional shift of the transition, the line center is actually closer to 1388.145 nm for typical conditions. While acceptable levels of absorption are still seen at 1388.139 nm, Figure 13 shows how this laser wavelength has an adverse effect on the uncertainty of the absorption coefficient. The variation of the absorption coefficient for the given conditions can be as much as 25% due to wavemeter uncertainty. This difference may explain some of the bias error seen in the corrected absorption coefficient results. If the laser were tuned to the true line center, the uncertainty would be significantly lower. In future experiments, care will be taken to ensure that the laser is truly on-line, at the conditions of the experiment and not necessarily at ambient conditions. An added benefit of having the laser on-line is that higher percent absorption will be achieved. In the example case, the absorption coefficient at line center is almost 2.5 times greater than at 1388.139 nm. This higher absorption would increase the SNR or alternatively would allow for higher-temperature tests to be performed while maintaining the current SNR since higher-temperature tests suffer from lower absorption coefficients.

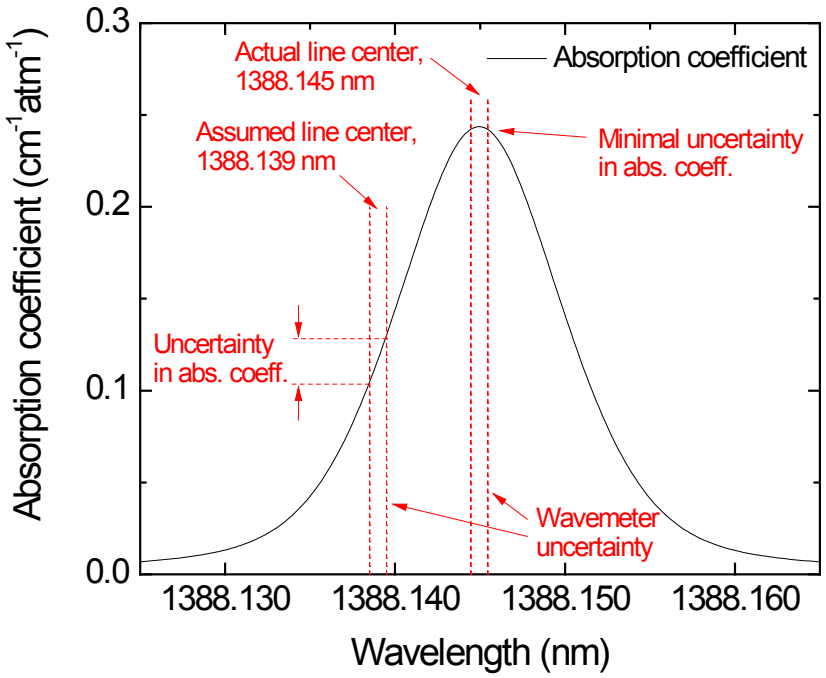

Figure 13. The actual wavelength used for these experiments contributed significantly to uncertainty in the absorption coefficient. Calculations are performed at 1450 K and 2.7 atm for a mixture of 0.5% H_2O and 99% Ar.

Third is the possibility of inaccurate data used to estimate γ_L, the Lorentzian HWHM. As mentioned previously, it has been determined that an appropriate ratio of the Ar-broadened HWHM to the N_2-broadened HWHM is 0.4 [30]. It has also been determined that the temperature exponent n used for N_2 can also be used for Ar, though one of the transitions studied showed a slight deviation in this regard. However, there are several things to note here. First, the four transitions studied by Nagali et al. were near 7117 cm^{-1} rather than the transition at 7204 cm^{-1} that was used in this study. This difference in wavenumber may or may not have an effect on the broadening parameters.

Second, the experiments performed to determine the ratio of 0.4 were only performed at 296 K. It seems likely that the broadening parameters of argon would be different at shock-tube conditions. Third, the experiments performed to determine the temperature exponent n were performed at temperatures from 350 to 473 K. Once again, this temperature range does not seem adequate for shock-tube measurements. A final note is that the Ar-broadening parameters were compared to the N_2-broadening parameters, not to the air-broadening parameters that HITRAN reports. Thus, using the Ar:N_2 ratios from Nagali et al. to correct the air-broadening parameters from HITRAN may be an inherently flawed method.

Ignition Delay Time Measurements

The comparison of kinetic profiles with models is inherently quite qualitative. A more quantitative comparison is the measurement of ignition delay times. This characteristic time is defined as the delay after achieving combustion conditions until combustion actually begins. The methodology for determining ignition delay time is demonstrated in Figure 14. In shock-tube experiments, time 0 is defined as the passage of the reflected shock wave, when the desired P_5 and T_5 conditions are reached. The time that combustion first begins is measured by matching the steepest portion of the rise in H_2O concentration with a straight line and extrapolating that line down to the baseline amount of H_2O.

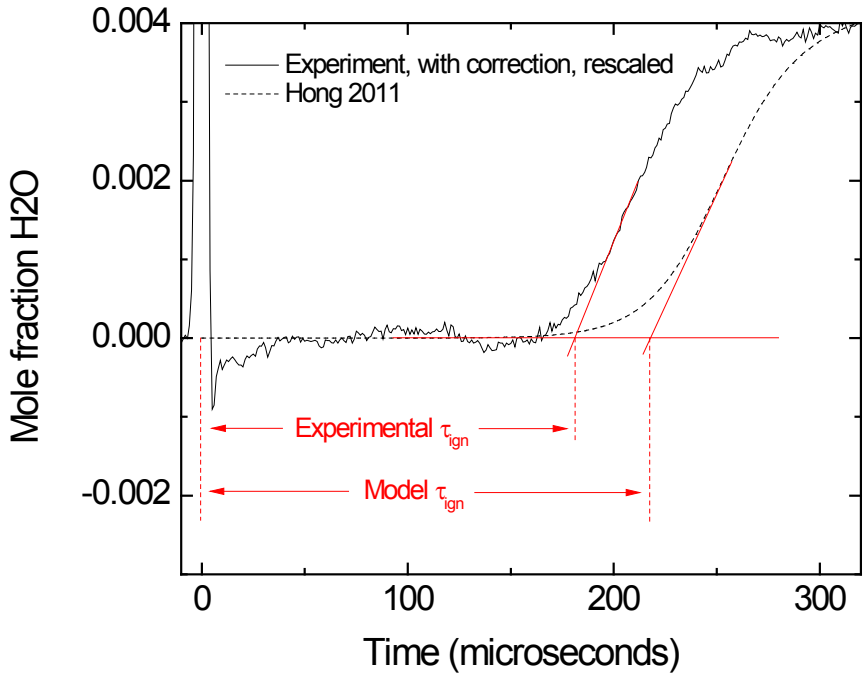

Figure 14. Methodology for defining experimental and model ignition delay times. Note that the noise in the signal makes defining the baseline difficult. Results shown are for a mixture of 0.33% O2, 0.67% H2, balance Ar at 1451 K and 2.751 atm.

Experimental versus predicted ignition delay times are shown in Figure 15. As is typical, the x-axis is plotted as 10000/T [K^{-1}], while the y-axis is a $\log_{10}$ scale of the ignition delay time [microseconds]. It is expected that the experimental data will fall along a straight line in such a plot. Such linear behavior is demonstrated, though the low-temperature runs (far right side of the plot) exhibit a deviation from linearity. Also, it is worth noting that the model over-predicts the ignition delay time in every case.

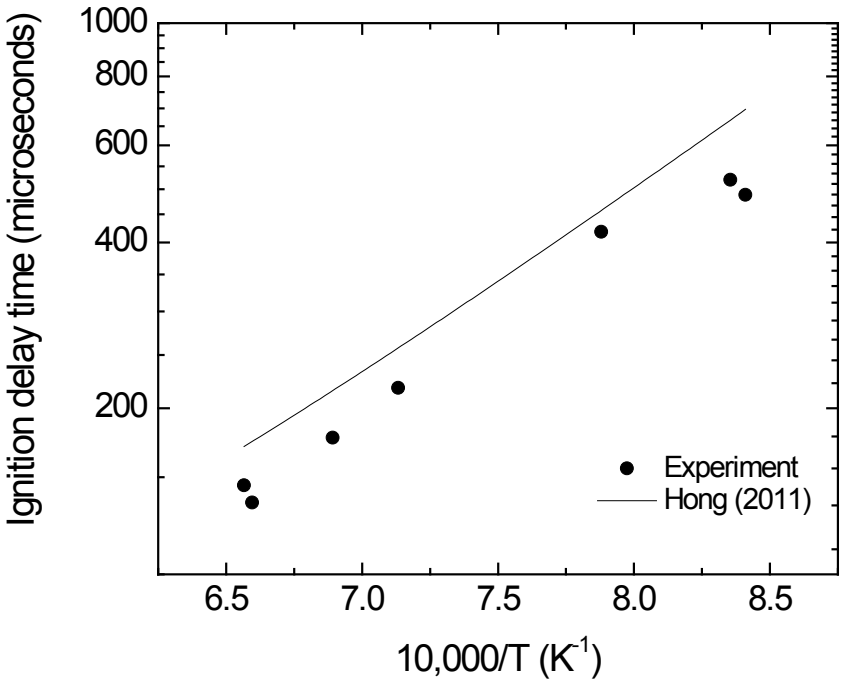

Figure 15. Experimental and modeled ignition delay times versus inverse temperature for the experiments performed in this study. The model over-predicts the data in every case. The y-axis is $\log_{10}$.

Similar ignition delay results have been observed by others. In the original paper from Hong et al., the model predictions had to be time-shifted slightly to match the data. While specific details as to the magnitude of the disagreement are not given, it is stated that trace amounts of hydrogen were added to the simulation environment to decrease the modeled ignition delay time. The fact that the model over-predicted the ignition delay is encouraging, as the same trend is observed in this study. One possible reason given for this inaccuracy is impurities within the shock tube [2]. Indeed, Davidson and Hanson have shown that small amounts of H_2 impurities can have a significant effect on

the ignition delay times of H_2 [42]. Thus, great care should be taken to ensure high purity within the shock tube. In the experiments performed, the shock tube was turbo-pumped for a minimum of 25 minutes before performing each test, although the ion gauge was not used to check the pressure. It is possible that by simply vacuuming down for a longer period of time, more accurate ignition delay times could be obtained. Another facet to this problem is the noise in the laser signal. This noise makes defining the baseline amount of H_2O more difficult. Reducing this noise level may serve to reduce uncertainty in determination of the ignition delay time.

However, it should be pointed out that the deviation between model and experiment in Figure 15 may not be due (at least entirely) to impurities. Note that the data seem to follow a consistent trend, while if one were to suspect impurities, it might seem reasonable to expect non-repeatability in the data. One would also expect to see a relationship between pumping time and the difference between model and experiment. Such considerations should be examined in future studies.

CHAPTER V

SUMMARY AND FUTURE WORK

The laser diagnostic has been shown to provide useful measurements of H_2O concentrations in a shock tube. However, several key points still need to be addressed.

1. *Signal-to-noise ratio*. The SNR in these experiments is acceptable but could still be improved. Beam steering is present in most every run, as evident by the fluctuations in signal after the reflected shock. This problem could be remedied by more precise alignment of the laser.
2. *Ar-broadening parameters.* The spectroscopic parameters of Ar-broadened H_2O are suspect and should be more closely investigated. The ratio of the air-broadened HWHM to the Ar-broadened HWHM could be better established by measurements at room temperature. The temperature exponent could be established by obtaining absorption profiles at appropriate shock-tube conditions. Such profiles could be obtained by repeating the same shock-tube conditions and progressively scanning the laser across the transition of interest. The collisional shift parameter could also be investigated to see if it is changed significantly due to the presence of Ar. This parameter could be obtained by performing shock-tube experiments across a range of pressures. One benefit of such tests is that lower values of T_5 can be sought. Traditionally, the low-temperature range of conditions is prohibited due to the ignition delay time of the mixture and the

limited test time of a shock tube. In these experiments, however, no chemical reaction needs to take place but only a change in absorption due to a change in temperature and pressure.

3. *Pre-shock noise in I and I_0*. About 7-8 milliseconds prior to the arrival of the incident shock, there is noticeable noise in both I and I_0. This noise contributes to uncertainty in the baseline amount of H_2O. One possible explanation is the vibration of the shock tube from the breakage of the diaphragm that travels through the steel tube faster than the shock wave. Better alignment of the optics may serve to mitigate the effects of this vibration.
4. *Effects of impurities*. When running future tests, great care will be taken to ensure that few impurities can enter the system. In order to determine the effects of impurities, tests could be performed in which the vacuuming time is varied to see if this has an effect on the ignition delay. It may be observed that the experimental ignition delay time continues to lie underneath the model predictions, in which case changes to the model would be proposed.

Future work will involve addressing the key issues mentioned in the previous paragraph. It will also involve performing measurements on various other combustion systems besides the H_2/O_2 system. Any hydrocarbon system produces H_2O as a byproduct, and thus this diagnostic has many potential applications. It is worth noting that not all hydrocarbon systems can use this diagnostic. The shock tube test time is typically around 2 ms, and thus ignition must occur well before this time limit expires.

For less reactive fuels, the temperature of the system must be high to achieve this. Since for this H_2O transition it is known that higher temperatures have an adverse effect on the absorption coefficient, some fuels may not be able to use this diagnostic due to low SNR. One method with which to extend the applicability of this diagnostic is to use a different laser. The absorption of H_2O near 2.5 microns is nearly an order of magnitude greater than that at 1.4 microns. Such a drastic increase in absorption would allow for more fuels to be tested, and for higher-quality data to be obtained for fuels that are already accessible.

REFERENCES

1. Westbrook, C.K. and F.L. Dryer, *Chemical kinetic modeling of hydrocarbon combustion.* Progress in Energy and Combustion Science, 1984. **10**(1): p. 1-57.

2. Hong, Z., D.F. Davidson, and R.K. Hanson, *An improved H2/O2 mechanism based on recent shock tube/laser absorption measurements.* Combustion and Flame, 2011. **112**: p. 633-644.

3. Konnov, A., *Remaining uncertainties in the kinetic mechanism of hydrogen combustion.* Combustion and Flame, 2008. **152**(4): p. 507-528.

4. Li, J., *An updated comprehensive kinetic model of hydrogen combustion.* International Journal of Chemical Kinetics, 2004. **36**(10): p. 566-575.

5. Ó Conaire, M., *A comprehensive modeling study of hydrogen oxidation.* International Journal of Chemical Kinetics, 2004. **36**(11): p. 603-622.

6. Smith, G.P., et al. *GRI-Mech 3.0*. 1999 [cited 2015 February 9].

7. Metcalfe, W.K., et al., *A hierarchical and comparative kinetic modeling study of C1–C2 hydrocarbon and oxygenated fuels.* International Journal of Chemical Kinetics, 2013. **45**(10): p. 638-675.

8. Davidson, D., *Recent advances in shock tube/laser diagnostic methods for improved chemical kinetics measurements.* Shock Waves, 2009. **19**(4): p. 271-283.

9. Fomin, N.A., *110 years of experiments on shock tubes.* Journal of Engineering Physics and Thermophysics, 2010. **83**(6): p. 1118-1135.

10. Payman, W., *Explosion waves and shock waves. Part II. The shock wave and explosion products sent out by blasting detonators.* Proceedings of the Royal Society of London. Series A, Mathematical and physical sciences, 1935. **148**(865): p. 604-622.

11. Payman, W., *Explosion waves and shock waves. Part III. The initiation of detonation in mixtures of ethylene and oxygen and of carbon monoxide and oxygen.* Proceedings of the Royal Society of London. Series A, Mathematical and physical sciences, 1935. **152**(876): p. 418-445.

12. Payman, W., *Explosion waves and shock waves. Part IV. Quasi-detonation in mixtures of methane and air.* Proceedings of the Royal Society of London. Series A, Mathematical and physical sciences, 1937. **158**(894): p. 348-367.

13. Payman, W., *Explosion waves and shock waves. Part VI. The disturbance produced by bursting diaphragms with compressed air.* Proceedings of the Royal Society of London. Series A, Mathematical and physical sciences, 1946. **186**(1006): p. 293-321.

14. Gaydon, A.G.H., I.R., *The shock tube in high-temperature chemical physics*. 1963, New York: Reinhold Pub. Corp. 307.

15. Bleakney, W., *The shock tube: A facility for investigations in fluid dynamics.* Review of Scientific Instruments, 1949. **20**(11): p. 807-815.

16. Bleakney, W. and A.H. Taub, *Introduction of shock waves.* Reviews of Modern Physics, 1949. **21**: p. 11.

17. Bleakney, W., D.R. White, and W.C. Griffith, *Measurement of diffraction of shock waves and resultant loading of structures.* Journal of Applied Mechanics, 1950. **17**(4): p. 7.

18. Glass, I.I. and G. Hall, *Handbook of supersonic aerodynamics, Section 18, Shock tubes*. Vol. 6. 1958, Silver Spring, MD.

19. Bauer, S.H., G.L. Schott, and R.E. Duff, *Kinetic studies of hydroxyl radicals in shock waves. I. The decomposition of water between 2400° and 3200°K.* The Journal of Chemical Physics, 1958. **28**(6): p. 1089-1096.

20. Lapp, M., *Shock-tube measurements of the f-number for the (0, 0)-band of the OH 2* $\sum \rightarrow$ *2* Π *transitions.* Journal of Quantitative Spectroscopy & Radiative Transfer, 1961. **1**(1): p. 30-45.

21. Hanson, R.K., *Absorption of CO laser radiation by NO.* Journal of Quantitative Spectroscopy & Radiative Transfer, 1976. **16**(8): p. 705-713.

22. Hanson, R.K., *Shock tube spectroscopy: advanced instrumentation with a tunable diode laser.* Applied Optics, 1977. **16**(6).

23. Flower, W.L., R.K. Hanson, and C.H. Kruger, *Experimental study of nitric oxide decomposition by reaction with hydrogen.* Combustion Science and Technology, 1977. **15**: p. 14.

24. Hanson, R.K., *Temperature measurement technique for high-temperature gases using a tunable diode laser.* Applied Optics, 1978. **17**(16): p. 2477-80.

25. Kychakoff, G., *Quantitative visualization of combustion species in a plane.* Applied Optics, 1982. **21**(18): p. 3225-7.

26. Rea, E.C., *Rapid-tuning frequency-doubled ring dye laser for high resolution absorption spectroscopy in shock-heated gases.* Applied Optics, 1984. **23**(11): p. 1691-4.

27. Eng, R.S.M., A. W., *Tunable diode laser measurements of H2O and Co2 line parameters in the 10-15 micrometers spectral region.*, 1978, United States Defense Technical Information Center.

28. Salimian, S.H., R.K., *Absorption measurements of H2O at high temperatures using a CO laser.* Journal of Quantitative Spectroscopy & Radiative Transfer, 1983. **30**(1): p. 1-7.

29. Webster, C.M., R., *Simultaneous in situ measurements and diurnal variations of NO, NO2, O3, jNO2, CH4, H2O, and CO2 in the 40- to 26-km region using an open path tunable diode laser spectrometer.* Journal of Geophysical Research, 1987. **92**: p. 11931-11950.

30. Nagali, V., *Measurements of temperature-dependent argon-broadened half-widths of H2O transitions in the 7117 cm(-1) region.* Journal of Quantitative Spectroscopy & Radiative Transfer, 2000. **64**(6): p. 651-655.

31. Baer, D.S., *Scanned- and fixed-wavelength absorption diagnostics for combustion measurements using multiplexed diode lasers.* AIAA Journal, 1996. **34**(3): p. 489-493.

32. Zhou, X., *Development of a fast temperature sensor for combustion gases using a single tunable diode laser.* Applied Physics B, Lasers and Optics, 2005. **81**(5): p. 711-722.

33. Hong, Z., *Hydrogen peroxide decomposition rate: A shock tube study using tunable laser absorption of H2O near 2.5 μm.* The Journal of Physical Chemistry A, 2009. **113**(46): p. 12919-12925.

34. Hong, Z., *Experimental study of the rate of OH + HO2 → H2O + O2 at high temperatures using the reverse reaction.* The Journal of Physical Chemistry A, 2010. **114**(17): p. 5520-5.

35. Hong, Z., et al., *A new shock tube study of the H + O2 → OH + O reaction rate using tunable diode laser absorption of H2O near 2.5 μm.* Proceedings of the Combustion Institute, 2010. **33**: p. 309-316.

36. Gharavi, M., *Single diode laser sensor for wide-range H 2 O temperature measurements.* Applied Spectroscopy, 2004. **58**(4): p. 468-473.

37. Rothman, D.C. and L.S. Rothman, *The HITRAN 2004 molecular spectroscopic database.* Journal of Quantitative Spectroscopy & Radiative Transfer, 2005. **96**(2): p. 139-204.

38. Rothman, L.S. *JavaHAWKS Manual*. 2004 [cited 2015 March 4].

39. Rothman, L.S., *The HITRAN molecular spectroscopic database and HAWKS (HITRAN Atmospheric Workstation): 1996 edition.* Journal of Quantitative Spectroscopy & Radiative Transfer, 1998. **60**(5): p. 665-710.

40. Whiting, E.E., *An empirical approximation to the Voigt profile.* Journal of Quantitative Spectroscopy & Radiative Transfer, 1968. **8**(6): p. 1379-1384.

41. Vivanco, J.E., *A new shock-tube facility for the study of high-temperature chemical kinetics*, in *Department of Mechanical Engineering*2014, Texas A&M University.

42. Davidson, D.F., *Interpreting shock tube ignition data.* International Journal of Chemical Kinetics, 2004. **36**(9): p. 510-523.

APPENDIX

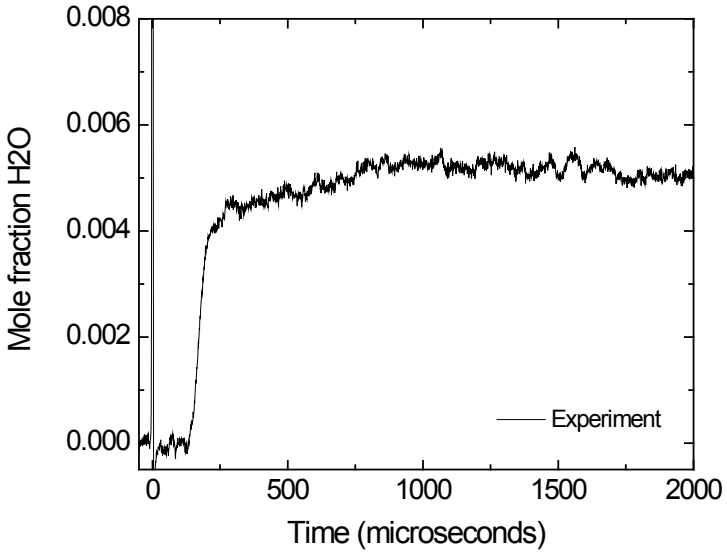

Figure A1. 1523 K and 2.674 atm in 0.33% O_2, 0.66% H_2, balance Ar.

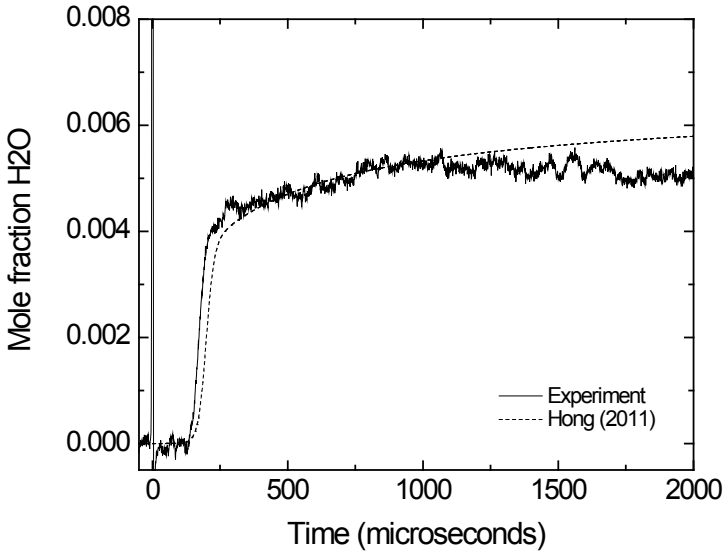

Figure A2. 1523 K and 2.674 atm in 0.33% O_2, 0.66% H_2, balance Ar. Compared with model predictions.

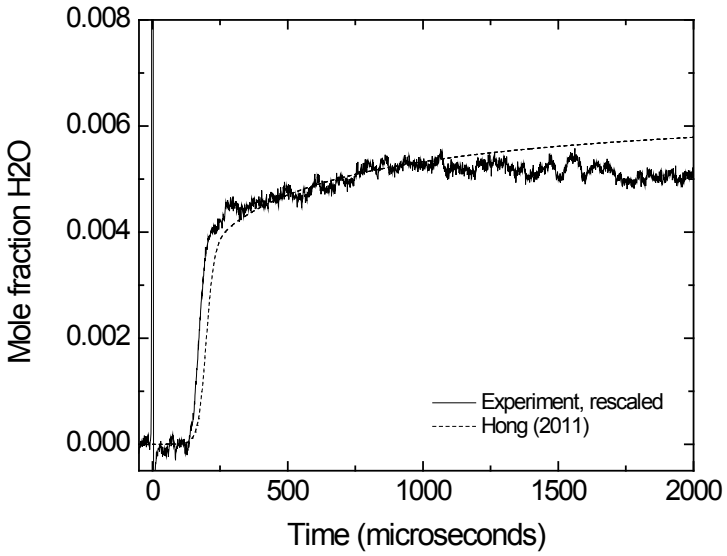

Figure A3. 1523 K and 2.674 atm in 0.33% O_2, 0.66% H_2, balance Ar. Compared with model predictions. Data rescaled.

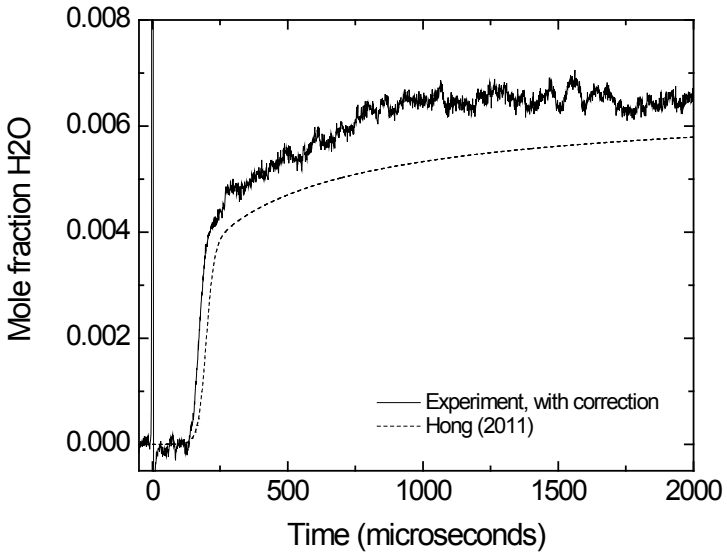

Figure A4. 1523 K and 2.674 atm in 0.33% O_2, 0.66% H_2, balance Ar. Compared with model predictions. Absorption coefficient correction applied.

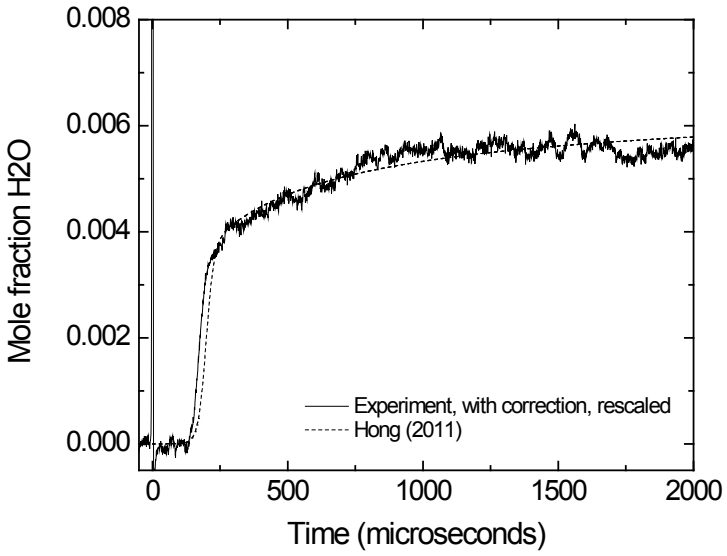

Figure A5. 1523 K and 2.674 atm in 0.33% O_2, 0.66% H_2, balance Ar. Compared with model predictions. Absorption coefficient correction applied. Data rescaled.

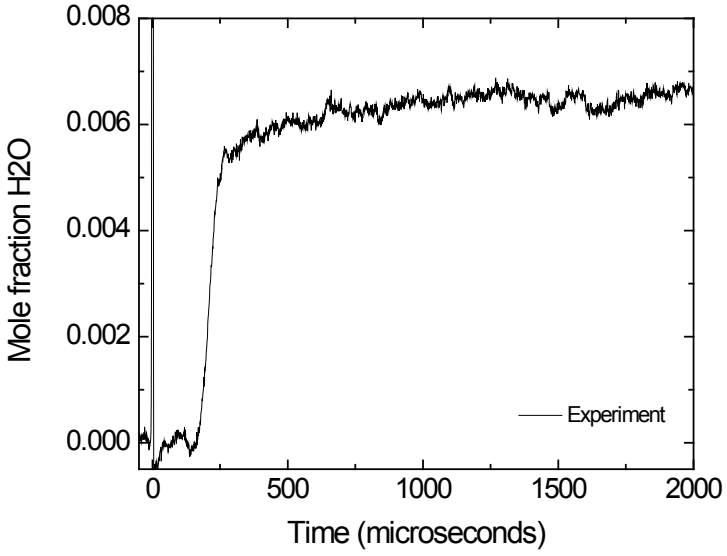

Figure A6. 1451 K and 2.751 atm in 0.33% O_2, 0.66% H_2, balance Ar.

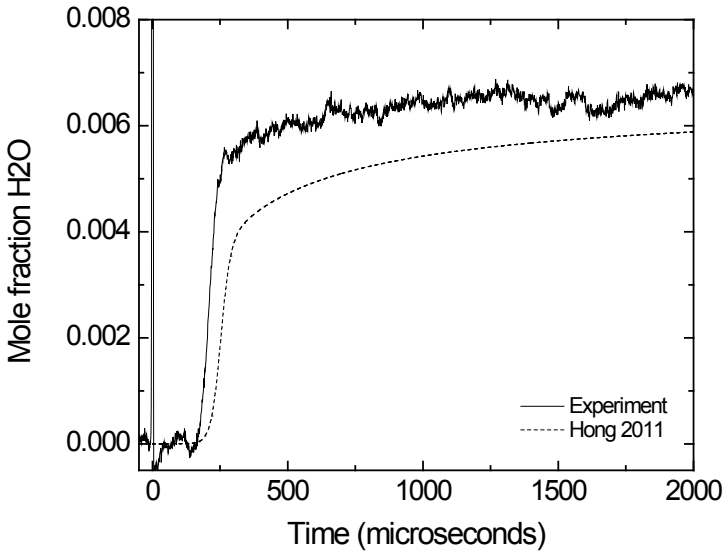

Figure A7. 1451 K and 2.751 atm in 0.33% O_2, 0.66% H_2, balance Ar. Compared with model predictions.

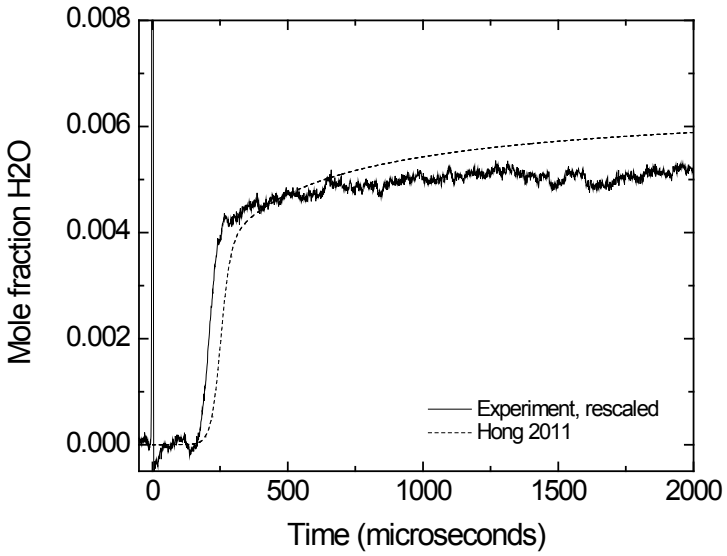

Figure A8. 1451 K and 2.751 atm in 0.33% O_2, 0.66% H_2, balance Ar. Compared with model predictions. Data rescaled.

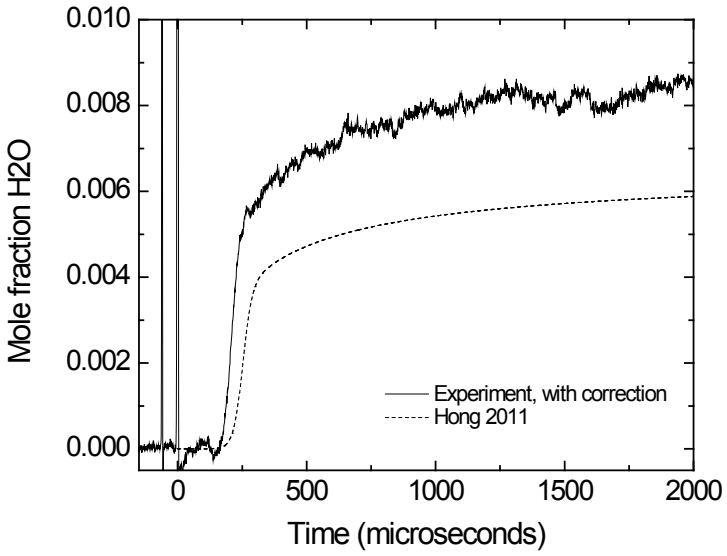

Figure A9. 1451 K and 2.751 atm in 0.33% O_2, 0.66% H_2, balance Ar. Compared with model predictions. Absorption coefficient correction applied.

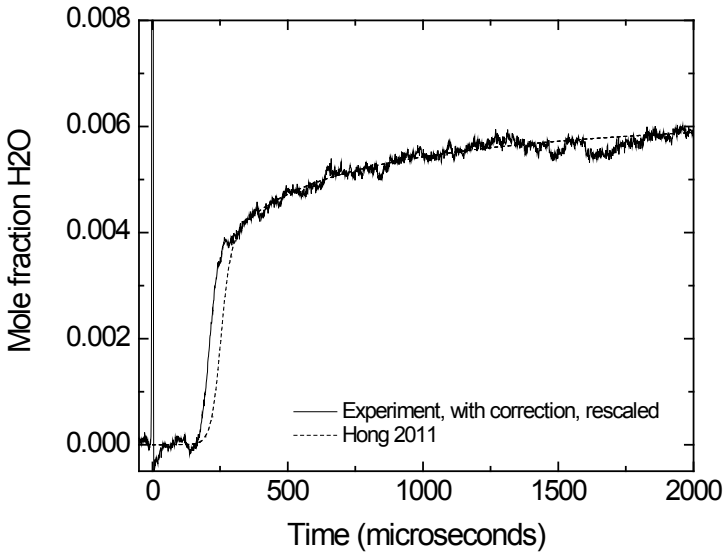

Figure A10. 1451 K and 2.751 atm in 0.33% O_2, 0.66% H_2, balance Ar. Compared with model predictions. Absorption coefficient correction applied. Data rescaled.

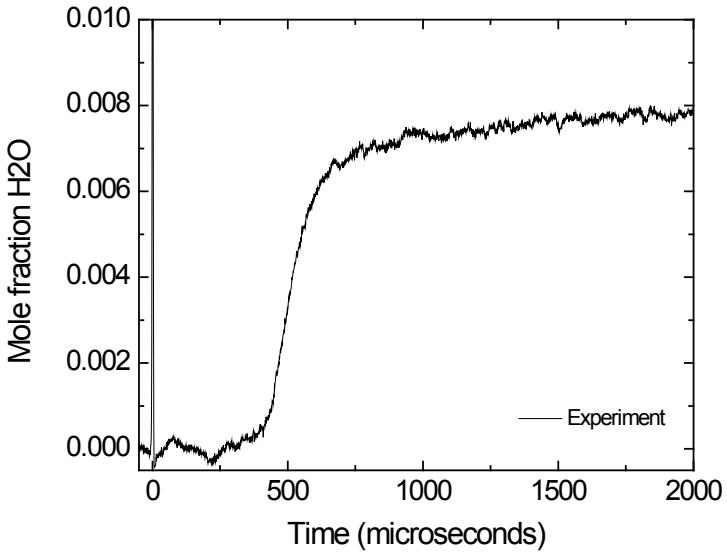

Figure A11. 1269 K and 2.929 atm in 0.33% O_2, 0.66% H_2, balance Ar.

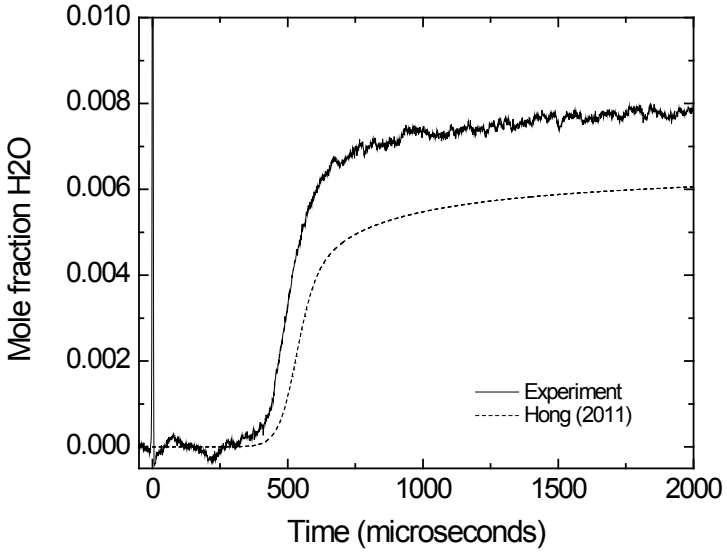

Figure A12. 1269 K and 2.929 atm in 0.33% O_2, 0.66% H_2, balance Ar. Compared with model predictions.

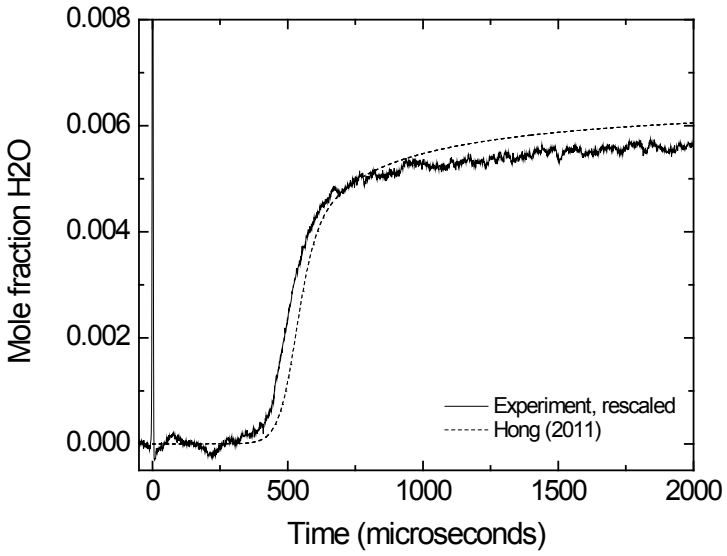

Figure A13. 1269 K and 2.929 atm in 0.33% O_2, 0.66% H_2, balance Ar. Compared with model predictions. Data rescaled.

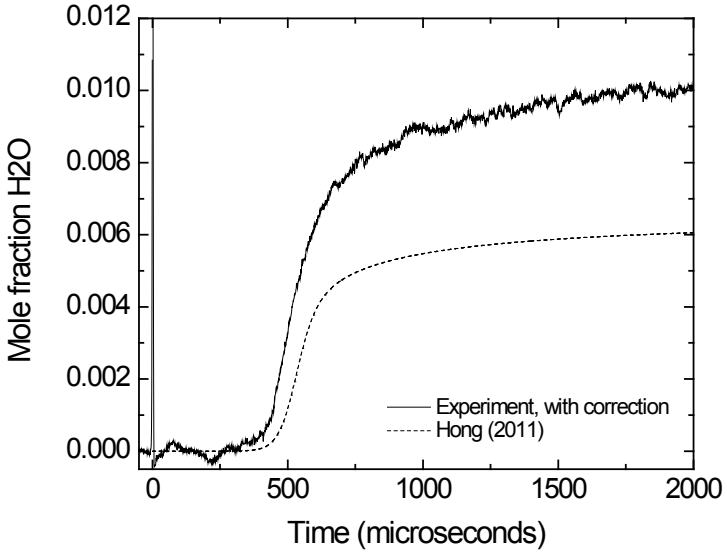

Figure A14. 1269 K and 2.929 atm in 0.33% O_2, 0.66% H_2, balance Ar. Compared with model predictions. Absorption coefficient correction applied.

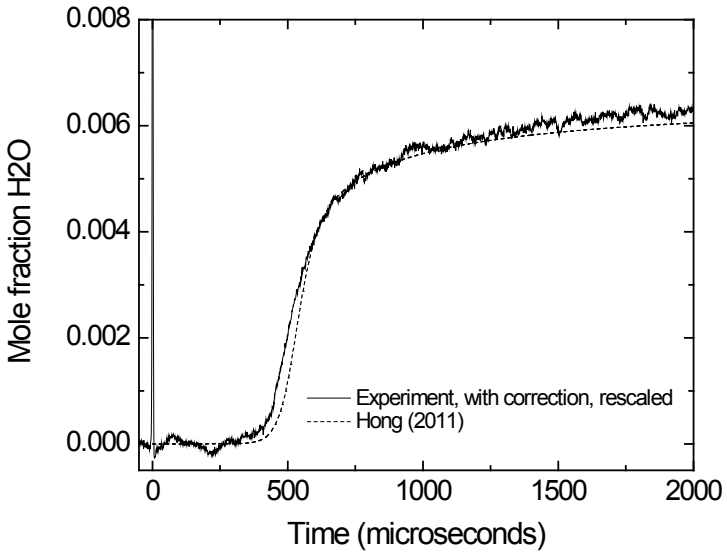

Figure A15. 1269 K and 2.929 atm in 0.33% O_2, 0.66% H_2, balance Ar. Compared with model predictions. Absorption coefficient correction applied. Data rescaled.

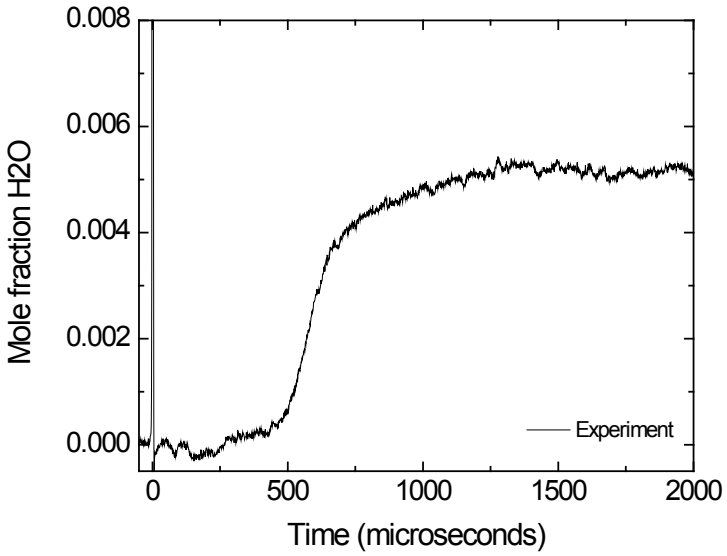

Figure A16. 1189 K and 3.087 atm in 0.33% O_2, 0.66% H_2, balance Ar.

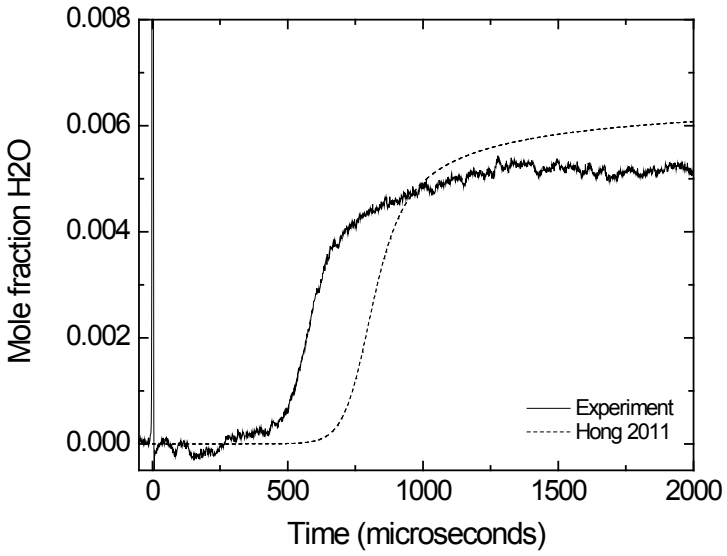

Figure A17. 1189 K and 3.087 atm in 0.33% O_2, 0.66% H_2, balance Ar. Compared with model predictions.

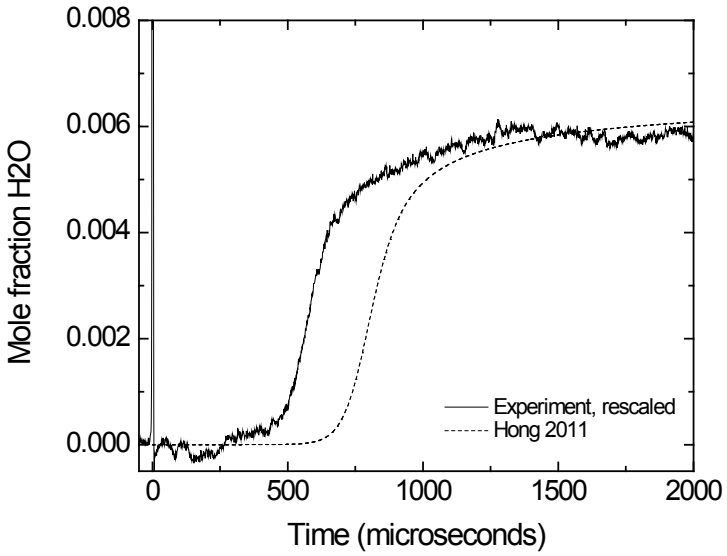

Figure A18. 1189 K and 3.087 atm in 0.33% O_2, 0.66% H_2, balance Ar. Compared with model predictions. Data rescaled.

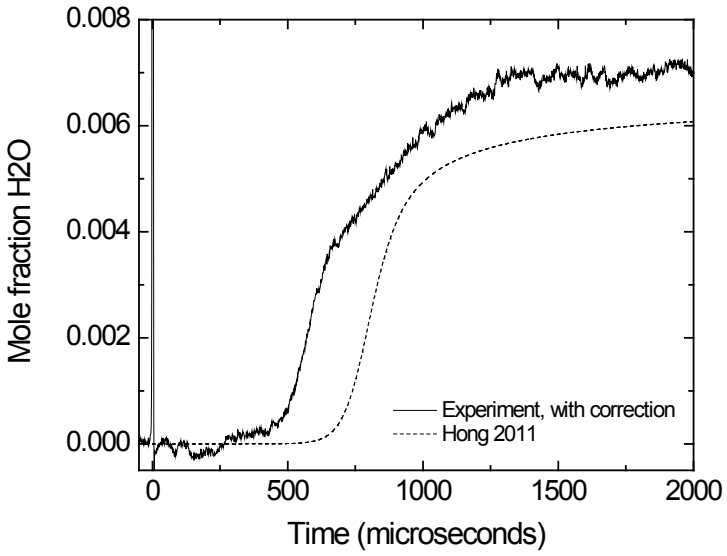

Figure A19. 1189 K and 3.087 atm in 0.33% O_2, 0.66% H_2, balance Ar. Compared with model predictions. Absorption coefficient correction applied.

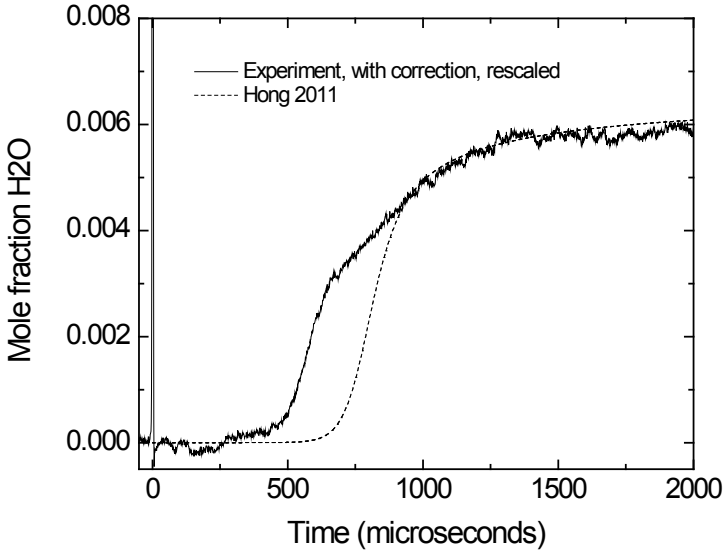

Figure A20. 1189 K and 3.087 atm in 0.33% O_2, 0.66% H_2, balance Ar. Compared with model predictions. Absorption coefficient correction applied. Data rescaled.